NTNU

Norwegian University of
Science and Technology

Texture and Microstructure Evolution during Extrusion of AlMgSi-Alloys

Helge Fylkesnes

Materials Science and Engineering
Submission date: June 2016
Supervisor: Knut Marthinsen, IMTE
Co-supervisor: Kai Zhang, IMT

Norwegian University of Science and Technology
Department of Materials Science and Engineering

Summary

The main objective of this work has been to contribute to a better understanding of the microstructure and texture evolution during and after extrusion of AlMgSi-alloys (AA6xxx-type alloy). The results can further be used as a basis for development of microstructure and texture models.

The textures and microstructures in AA6082 were analysed after extrusion into a flat profile, after extrusion into a cylindrical rod, after subsequent rolling of the extruded rod material and after annealing of the rolled plate. The textures and microstructures in AA6060 were analysed after extrusion into a cylindrical rod, after subsequent cold rolling of the extruded rod material and after annealing of the rolled plate material. The microsturctures and textures of these samples was investigated by Electron Back Scatter Diffraction (EBSD) in a scanning electron microscope (SEM) and by X-ray difractometry (XRD). The AA6060 extruded round rod had a recrystallised microtructure where the texture consistedd of partly $\langle 100 \rangle$-fibre coupled with a random texture. AA6082 extruded rod contains dispersoid which hinders recrystallisation. Thus the microstructure was a non-recrystallised microstructure consisting of 0.5 $\langle 100 \rangle$-fibre and 0.43 $\langle 111 \rangle$-fibre. The cold rolling was carried out on material having these textures.

Texture simulations were mainly carried out using Viscoplastic Self-Consistent model (VPSC). The parameters varied in these simulations were slip planes activated during deformation, strain rate sensitivity and interaction scheme. The deformation modes used during the simulations were uni-axial tensile deformation (Carried out using a random texture as input texture) and plane strain deformation (Carried out using $\langle 100 \rangle$-fibre and $\langle 111 \rangle$-fibre texture as input texture). Texture simulations were also done using ALAMEL model (and modifications of it). These simulations were carried out using the same deformation modes coupled with the same input textures as the VPSC simulation. Active slip systems and type of relaxation were varied in the ALAMEL simulations. These simulations were partly done to find what effect the different simulation parameters have one the end texture. They were also done to find how one can get the textures observed experimentally in aluminium (mainly high fraction of $\langle 100 \rangle$-fibre after extrusion of cylindrical rods and high amount of Cube components after extrusion of flat profiles).

The main findings were that inclusion of the $\{112\}\langle 110 \rangle$ slip system in texture simulations gives a texture closer to the experimental observed texture when the deformation mode were uni-axial tensile deformation. It was not possible to find simulations parameters, using plane strain deformation, which gave texture close to the experimental observed texture (high amount of Cube).

Sammendrag

Hovedmålet med denne masteroppgaven har vært å bidra til en bedre forståelse av mikrostruktur- og teksturutvikling under og etter ekstrudering av AlMgSi-legeringer (AA6xxx type legeringer). Resultatene kan brukes videre som basis for utvikling av mikrostruktur- og teksturmodeller.

Teksturer og mikrostrukturer ble analysert etter ekstrudering av en flat profil, etter ekstrudering til en rund stav, etter valsing av den runde staven og etter varmebehandling av den valsede platen. Teksturer og mikrostrukturer ble også analysert i AA6060 etter ekstrudering av en rund stav, etter påfølgende valsing og etter påfølgende varmebehandling. De nevnte teksturene og mikrostrukturene ble analysert ved bruk av Electron Back Scatter Difraction (EBSD) i skanning elektron mikroskop (SEM) og ved hjelp av røntgendiffraktometri (XRD). Den ekstruderte runde staven av AA6060 hadde en rekrystallisert mikrotruktur hvor teksturen bestod av $\langle 100 \rangle$-fiber og "random" tekstur. AA6082 inneholder dispersoider som hindrer rekrystallisering. Derfor har den extruderte staven av AA6082 en ikke-rekrystallisert mikrostruktur som består av 0.5 $\langle 100 \rangle$-fiber og 0.43 $\langle 111 \rangle$-fiber. Kaldvalsingen ble dermed utført på materialer som har disse teksturene.

Tekstursimulering ble hovedsakelig gjort ved bruk av Viscoplastic Self-Consistent model (VPSC). Parametrene som ble variert under disse simuleringene var aktive slipsystemer, tøyningsratesensitivitet og interaksjons metode. Deformasjonsmodene som ble brukt i simuleringene var strekk i en akse (Utført med en tilfeldig tekstur som inputtekstur) og plan skjærdeformasjon (Utført med $\langle 100 \rangle$-fiber og $\langle 111 \rangle$-fiber tekstur som input). Tekstursimulering ble også gjort ved bruk av ALAMEL (og modifikasjoner av den). Disse simuleringene brukte samme deformasjonsmode og inputtekstur som VPSC-simuleringene. Aktive slipsystem og type relaksjon ble variert i ALAMEL-simuleringene. Disse simuleringene var delvis gjort for å finne effekten av forskjellige simuleringsparametre på slutteksturen. De ble også gjort for å finne ut hvordan mann kan oppnå den eksperimentelt observerte texturen i aluminium (Hovedsaklig høyt innhold av $\langle 100 \rangle$-fiber etter ekstrudering av runde staver og høyt inhold av Cube komponenter etter ekstrudering av flate profiler.

Hoved fundndene var at mann ved å inkludere $\{112\}\langle 110 \rangle$ slipsystemet i tekstursimuleringer kan få en tekstur som er nærmere teksturen observert eksperimentelt ved strekk i en akse. Det var ikke mulig å finne simuleringsparametre som ga tekstur lik eksperimentelt observert tekstur ved bruk av plan skjærdeformasjon.

Preface

This master thesis are done as a part of a master in Material Technology at NTNU. The work done in this thesis is related to the COSMETEX project. The supervisor for this thesis was Knut Marthinsen and the co-supervisor was Kai Zhang.

I have received help from several persons during the writing of this thesis. I would firstly like to thank my supervisor Knut Marthinsen and my co-supervisor Kai Zhang for their help. They have helped me with the planning and analysing of both the experimental and the simulation work. They have also been extremely helpful in the writing of the thesis.

I would also like to thank Trygve Lindahl Schanche, Torild Krogstad and Yingda Yun for help with the experimental work done in this thesis.

Table of Contents

Chapter 1

Introduction

Aluminium has several properties that makes it suited as a structural material. These properties includes aluminium's low weight and specific strength, it's good corrosion properties, it's good formability and it's ability to be recycled. Due to the increased focus on recycling, environment friendly materials and light weight materials, an increasing use of aluminium has been recognised in the recent decades. Applications for aluminium products which are predicted to increase in the near future are, amogst others, upper range consumer electronic and household articles. These applications have in particular high requirements for surface appearance. All of the above mentioned properties are dependent on the composition of the alloy and the processing of the material, which includes casting, thermomechanical processing, machining and surface finishing.

Extrusion is a forming process which can be used to form aluminium to complex shapes in a fast and cost effectiv way. One problem in forming aluminium in this way is to control the microstructure during the process, so that one can get a homogeneous and consistent microstructure and texture along as well as across the profiles. Unevenness in the microstructure will appear as uneven coloring in the surface, especially after anodizing, which is a common surface treatment in aluminium applications where visual appearance is important.

The general scope and objective of the COSMETEX[1] project is to establish a better understanding and quantitative description of the microstructure and texture evolution during extrusion, with a special focus on dispersoid-free AlMgSi-alloys (i.e. 6060-type alloys), and in particular the final recrystallised grain structure and texture (incl. through thickness variations). The aim is to further develop and validate adequate physically based models for the prediction of grain structure and texture as a function of processing conditions (die shape, extrusion temperature, extrusion speed etc.) for these types of alloys. A particular challenge with AA6060-type alloys during extrusion, as they (mainly) do not contain dispersoids, which may hinder/retard recrystallisation, is that recrystallisation easily take place already at the exit of the die (spontaneous recrystallisation).

[1] The COSMETEX project is an IPN project co-funded by the Research council of Norway and the industrial partner SAPA, with SINTEF and NTNU as research partners.

As part of the COSMETEX project a laboratory scale extrusion press has been constructed at the SAPA R&D laboratory in Finspång, Sweden. This laboratory press can make round ($\sim$ 2 mm) as well as flat profiles ($\sim$ 2 mm thickness * 20 mm width). The extrusion set-up features an immediate water-quenching at the end of extrusion; quenching to below 300 °C within 2 s, which is implemented with the purpose of possibly being able to avoid spontaneous recrystallisation after extrusion and thus freeze the deformation structure of the AA6060-type alloy. Access to the deformation structure and texture is essential as they represent the key to understand and describe the subsequent recrystallisation behaviour, both with respect to grain structure/size and texture.

The present master project as well as the previous specialisation project (Fylkesnes (2015) is closely related to the COSMETEX project, in the sense that it (mainly) makes use of extruded profiles provided by the COSMETEX project and serve as a supplement to the experimental characterisation and modelling work carried out within the COSMETEX. In a previous specialisation project (Paulsen (2015) focus was mainly on the characterisation the deformation and annealing behaviour of round lab-scale profiles provided by SAPA. The original intention of the present master project was to focus on the lab-scale flat profiles (of AA6060) processed at the SAPA laboratory, including their deformation behavior as well as their recrystallization behavior upon subsequent annealing. It turned out however to be difficult/impossible to avoid spontaneous recrystallisation in the AA6060 flat extruded profiles from the SAPA lab. press, even after extrusion at fairly low temperatures and low extrusion speed.

The experimental work has therefore but somewhat re-oriented and has been focused on experiments of both round profiles of AA6060 as well as both round and flat profiles of AA6082 extruded at the SINTEF extrusion press in Trondheim, for which the dimensions are much larger than for the SAPA laboratory press (i.e. round profiles with diameter 20 mm and flat profiles 20 mm x 80 mm). Additional laboratory scale rolling of the larger round profiles (both AA6060 and 6082) has also been carried out. These experiments are motivated by recent findings in the COSMETEX project that during extrusion of round billets into flat profiles the deformation behaviour before entering the die resembles uniaxial tension followed by mainly plane strain compression deformation behaviour during the extrusion die. These experiments are also carried out in a search for the origin of the Cube texture component which often dominates the texture of recrystallised aluminium alloys (incl. the centre region of extruded flat profiles, both for AA6060 and AA6082 (e.g. Furu and Vatne (1998) as well as related COSMETEX-work (Zhang et al. (2015).

Recent work in the COSMETEX project has shown that predicting the deformation texture after extrusion, and in particular in flat profiles is challenging. An important object of the present master project has therefore also been to see how different crystal plasticity (CP) models (including the classical FC-Taylor model), different variants of the grain interaction model ALAMEL, and the Visco Plastic Self Consistent model (VPSC) perform in this respect.

Although mainly well established, these models are not always straight forward to use and involve a number of options and parameters to be set, to run the simulations, e.g. with respect to deformation mode(s), degree of deformation (strain), choice of active slip system, and strain rate sensitivity etc.

On this background the texture simulation work has been two-fold. Firstly it involves

a number of generic simulations using the different CP models with different choice of options and parameters to see how different options and parameters affect the texture predictions, and compare how the different model perform, i.e. a kind of (limited) model and parameter sensitivity analysis. Secondly the objective has been to explore which model/model options and what parameters seem best suited to reproduce the experimental texture evolution for different extrusion conditions, e.g. with respect to deformation mode (i.e. uni-axial tension vs plane strain compression) and extrusion/deformation temperature.

Parameters explored in this thesis include addition of several active slip systems, observed at high temperature, to the CP models. For VPSC different interaction schemes(also called linearisation schemes) and strain rate sensitivity are tested. With ALAMEL different relaxations of shear strain are varied. The different modeling parameters are mainly compared with regards to fraction $\langle 100 \rangle$-fibre with uni-axial tensile deformation and by strength of Cube component and of Goss component with plane strain deformation.

Chapter 2

Theory

2.1 Aluminium

Aluminium alloys can be categorised in different ways. Initially they are divided into cast alloys and wrought alloys. Cast alloys are casted to their final form. These alloys usually have a composition closer to the eutectic composition providing it a lover melting temperature and higher castability. Wrought alloys are alloys which are cast into billets before further processed by one or more of the following processes: rolling, extrusion and forging. Different alloys can be identified by the International Alloy Designation System (IADS). Cast aluminium designation system is shown in Table 2.1 and wrought aluminium alloy designation system is shown in Table 2.2 (Davis and Davis (1993). Wrought alloys can further be divided into alloys that can be hardened by heat treatment (so called heat treatable alloys e.g. 2xxx, 6xxx and 7xxx) and alloys that cannot (non-heat treatable alloys e.g. 3xxx and 5xxx).

Table 2.1: Numeration of different cast alloy series

Composition	**Series**
Pure aluminium (>90%)	1xx.x
Copper	2xx.x
Silicon with added copper and/or magnesium	3xx.x
Silicon	4xx.x
Magnesium	5xx.x
Zinc	6xx.x
Tin	7xx.x
Other elements	8xx.x

Table 2.2: Numeration of different wrought alloy series

Composition	Series
Pure aluminium (>90%)	1xxx
Copper	2xxx
Manganese	3xxx
Silicon	4xxx
Magnesium	5xxx
Magnesium and silicon	6xxx
Zinc	7xxx
Other elements	8xxx

2.1.1 6000-Series

The 6000-series of wrought Al alloys contain commonly used alloys. In 2006 it accounted nearly 75% of aluminum used in extrusion. It contains magnesium and silicon as the main alloying elements. The inclusion of these elements gives the 6000- series the ability to be hardened by heat treatment. Mg and Si containing precipitates have proved to form during heat treatment. The process of this precipitation is commonly believed to be as following (Miao and Laughlin (1999):$\alpha \rightarrow$ GP-zones$\rightarrow \beta'' \rightarrow \beta' \rightarrow \beta$ with a more refined form as $\alpha \rightarrow$ GP-zones$\rightarrow \beta'' \rightarrow \beta'$, U1, U2,$\beta'' \rightarrow \beta$, Si, (Marioara et al. (2005), Matsuda et al. (2000), Marioara et al. (2006), Edwards et al. (1998). Except for the equilibrium phase β with composition Mg_2Si, and Si, all phases are metastable.

Historically, all the precipitates, including β'', were assumed to have the Mg_2Si composition. However, it is now well known that the β'' precipitates do not have the stochiometric ratio Mg_2Si, but closer to Mg_5Si_6 (Andersen et al. (1998). Recent work have shown that the β''-precipitates also may include some Al, with a suggested composition close to $Mg_5Al_2Si_2$ (Hasting et al. (2009). The alloy is strongest when the precipitates is a mix between GP-zones and β'' (Andersen et al. (1998).

AA6082

AA6082 is a high to medium strength aluminium alloy commonly used for extrusion. In 2000 8.9% of all extruded products where made using this alloy (Reiso (2004). As seen in table 2.3 AA6082 has a high amount of manganese which is added to create manganese containing dispersoids. These dispersoids are formed during the homogenisation process and are added to prevent recrystallisation (Hu et al. (2010).

AA6060

AA6060 is a medium strength aluminium alloy which is easy to extrude into profiles with complex cross-sections. The composition of this alloy is given in Table2.3. This alloy contains no or a limited amount of dispersoids and is therefore more susceptible for recrystallisation.

Table 2.3: Limits for the competition of AA6082 (aalco.co.uk (2016a) aalco.co.uk (2016b).

Chemical Element	% AA6082	% AA6060
Manganese (Mn)	0.40 - 1.00	0.0 - 0.10
Iron (Fe)	0.0 - 0.50	0.10 - 0.30
Magnesium (Mg)	0.60 - 1.20	0.35 - 0.60
Silicon (Si)	0.70 - 1.30	0.30 - 0.60
Copper (Cu)	0.0 - 0.10	0.0 - 0.10
Zinc (Zn)	0.0 - 0.20	0.0 - 0.15
Titanium (Ti)	0.0 - 0.10	0.0 - 0.10
Chromium (Cr)	0.0 - 0.25	0.0 - 0.05
Other (Each)	0.0 - 0.05	0.0 - 0.05
Others (Total)	0.0 - 0.15	0.0 - 0.15
Aluminium (Al)	Balance	Balance

2.2 Thermo-mechanical processing

Thermo-mechanical processing is a collective term for processes where a material is effected by mechanical deformation and elevated temperatures. Examples of this are extrusion, rolling and forging. The thermo-mechanical processing allows forming a metal billet into complex shapes, while increasing the mechanical properties of the material.

An example of a thermo-mechanical processing path for an extruded aluminium product is shown in Figure 2.1 and Figure 2.2. The metal is casted into a billet having the desired composition of the end product. The billet is then homogenised to get rid of low melting point eutectic phases, level out segregations, transform non-equilibrium phases into stable phases, spherodise insoluble phases and control the formation of dispersoid particles (Reiso (2015). The billet is then preheated to get desired temperature for extrusion. The billet is then extruded to get the desired geometry. The temperature increases during the extrusion because of the work used to form the metal. After extrusion the extrudate is cooled to control recovery, recrystallisation and grain growth in the extruded profile if possible. It is also done to control the precipitation of secondary phases. Last step in this process diagram is ageing where the aluminium is annealed at elevated temperature to strengthen the product by precipitation strengthening.

2.2.1 Extrusion

Extrusion is a commonly used process for making half-fabricates such as profiles and tubes from cast billets. The process is done by pressing the billet through a die having the desired geometry of the extrudate. Extrusion is mostly used on heated metal for reduced billet strength, which reduces the required force for the extrusion press.

The extrusion ratio (R_{ext}) is described by the ratio between the radius of the extrusion billet (A_0) and the radius of the cross section to the extruded product (A_f): $R_{ext} = A_0/A_f$. The average strain can be approximated by $\bar{\epsilon} = ln(R_{ext})$. Strain varies depending on the position in the extruded profile. Fem simulation by presented in chapter 4.2.1 shows that the deformation mode in the centre of extruded round profiles is near uni-axial

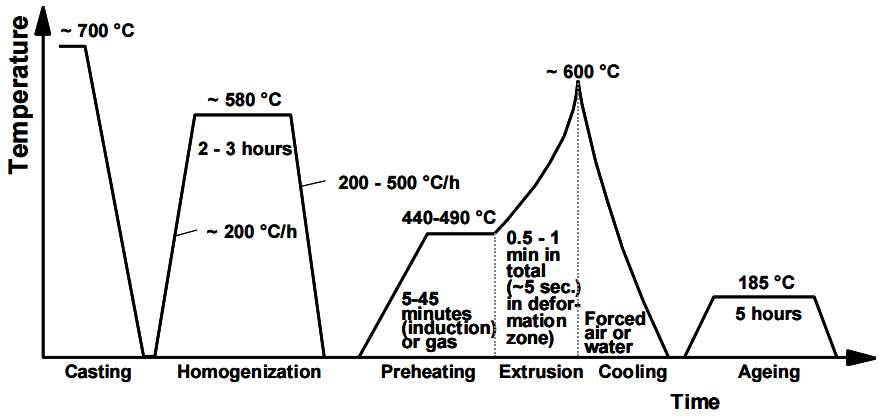

Figure 2.1: Common processing path for thermo-mechanical processing(Reiso (2004).

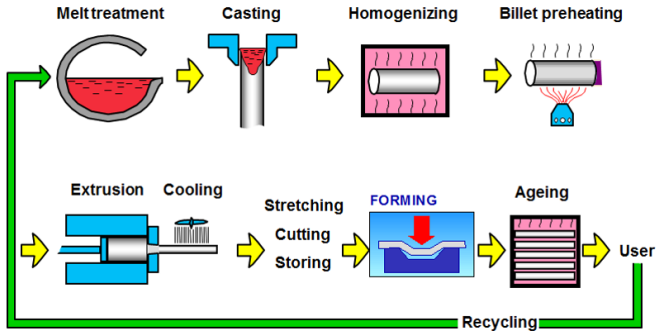

Figure 2.2: Full process form melting to finished product using extrusion(Reiso (2015).

elongation. The center of rectangular shaped extruded profiles is first close to that of a round profile. At later stages of the extrusion it will change to be closer to plane strain deformation. The region near the surface of extruded plates experience shear deformation components in addition to the plane strain components (Verlinden et al. (2007).

2.2.2 Rolling

Rolling is a forming process where a rectangular billet pass between rolls which deform the billet during the pass. During a rolling process the thickness of the billet is reduced. The width of the rolled billet stays roughly the same during the rolling, meaning that the volume is mainly preserved by elongation of the billet.

Reduction from rolling is given by equation 2.1. Here h_0 is the initial thickness and h_f the end thickness. True strain is given by equation 2.2 (Verlinden et al. (2007).

$$r = \frac{h_0 - h_f}{h_0} \tag{2.1}$$

$$\bar{\epsilon} = \ln\left(\frac{h_0}{h_f}\right) \tag{2.2}$$

2.2.3 Microstructure evolution

During thermo-mechanical processing like rolling and extrusion the microstructure will go through significant. In the as cast and homogenised state the microstructure will consist of fairly large equiaxed grains with no preferred grain orientations (random/no texture). During large (plastic) deformation the initial grain structure will be distorted where the grains largely will change shape according to the macroscopic change in the subjects dimensions during the relevant deformation process (e.g. rolling or extrusion), causing the grains to become flattened and elongated (as schematically illustrated Figure 2.3 **(a)**. Most of the energy that is generated during the deformation process is released as heat, but anything from 1-10% of the energy may be stored in the structure of the material, mainly in the form of line defects, i.e. dislocations.

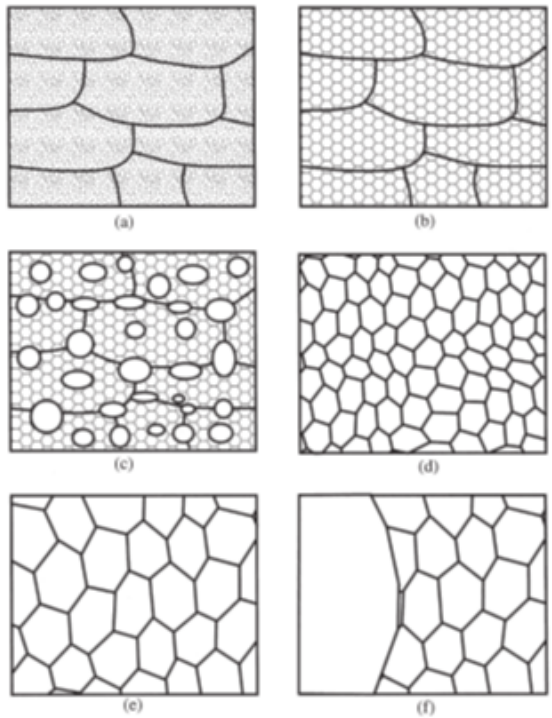

Figure 2.3: Schematic diagram of the main annealing processes; **(a)** Deformed state, **(b)** Recovered, **(c)** Partially recrystallised, **(d)** Fully recrystallised, **(e)** Grain growth and **(f)** Abnormal grain growth. (From Humphreys and Hatherly (2004).

Different substructures may arise during deformation, depending on the material and the parameters of the process. Aluminium is a high stacking fault energy material, and cellular substructures rather than twins and stacking faults are generally formed. The sub-structures that develop are temperature dependent. At low temperatures cellular structures are likely to form, while at higher temperatures sub-grains with narrow well-defined walls are the most likely (Figure 2.3 **(b)**.

The deformation structures during or after thermo-mechanical processing are thermo-dynamically unstable, such that upon subsequent annealing (or spontaneously if already at a high temperature) different thermally activated processes will be activated, which will lead to an evolution of the sub-structure driven by the stored energy in the structure. The processes and microstructure reactions leading to the changes during heat-treatment may be separated into:

- Recovery in which annihilation and rearrangement of dislocations will take, i.e. the formation of a well-defined substructure as illustrated in Figure 2.3 **(b)**, and possible homogeneous growth of this sub-grain structure (sub-grain growth).
- Recrystallization which refers the formation of (nucleation) of new dislocation-free grains and the gradual consumption of the cold worked matrix by growth of these grains (by migration of high-angle grain boundaries) (see Figure 2.3 **(c)** and **(d)**.
- Grain growth in which the fully recrystallization grain structure evolves by further migration of the high angle grain boundaries as to reduce he total grain boundary area (2.3 **(c)**.

Recovery and recrystallization may also take place during deformation, and is typical for aluminum. It is then called dynamic recovery and dynamic recrystallization. Recovery and recrystallization are kind of competing processes, and their relative amount depends on several factors, e.g. strain, annealing temperature and material. In general, recovery is the dominant mechanism at lower temperatures and as the temperature increases recrys-tallization becomes more dominant (further explained in Chapter 2.5 below).

2.3 Texture

Crystallographic texture is the statistical distribution of grain orientations in a metal. Grain orientation is the orientation of a crystal unit cell relative to an external coordinate system. For an extruded profile this coordinate system has axes parallel to the extrusion direction, the normal and the transverse direction, respectively, of a flat profile as shown in Figure 2.4.

2.3.1 Pole figure

A pole figure shows the stereographic projection of one orientation in a deformed metal (e.g. $\langle 100 \rangle$ or $\langle 111 \rangle$) in a crystal. How the projection work can be illustrated by putting the sample in the centre of a unit sphere. For rolled metal and flat extruded profiles the normal direction (ND) of the structure are pointing toward the north pole of the sphere. A

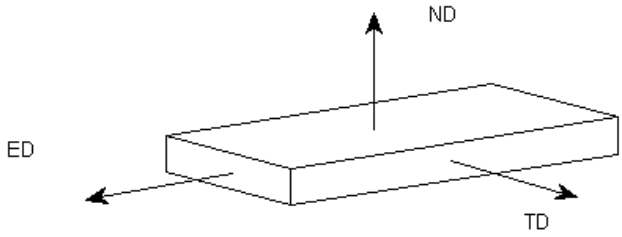

Figure 2.4: Directions in a flat extruded profile

crystal in a grain has a certain orientation in the macroscopic co-ordinate system, which means that a characteristic direction in the crystal's co-ordinate system (e.g. $\langle 100 \rangle$ and $\langle 100 \rangle$) has a certain orientation in the macroscopic co-ordinate system. The pole figure is built by drawing a line, which is parallel to a characteristic direction, from the centre pole of a sphere. This line will intercept the sphere on the northern hemisphere. A line is drawn between the south pole of the sphere and the intersection point. The pole figure is where this line intersects with the equatorial plane as shown in Figure 2.5. One pole figure is unique to a crystallographic orientation of a grain and the chosen crystal direction. By combining the pole figures of all grains in a structure we get a figure that shows the overall texture of the structure represented as a pole figure of a certain direction.

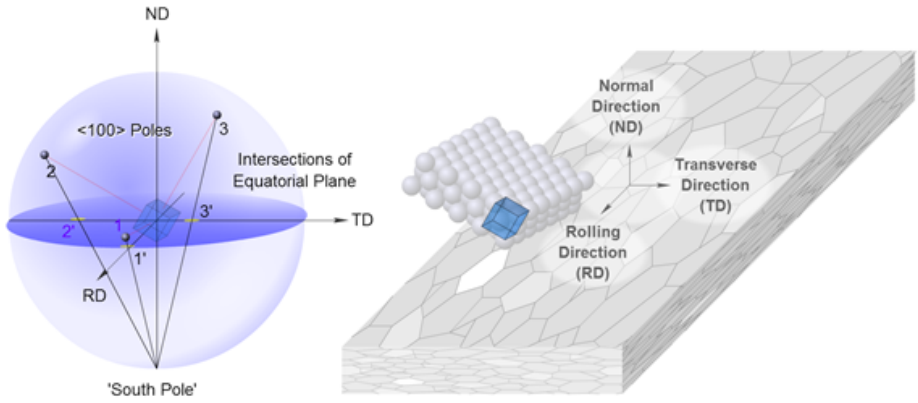

Figure 2.5: Stereographic representation of a pole figure. The pole figure shows where the lines intersects the ED-TD plane(AluMatter (2016)).

2.3.2 Euler angles and Euler space

Euler angles are a set of three angles which describe the orientation of a grain rotated from a "cube" position. The first angle (ϕ_1) describes the rotation around the original z-axis.

The second angle(Φ) describes the rotation around the rotated x-axis. The third angle (ϕ_2) describes the rotation around the rotated z-axis. To get the rotated cube, the cube is rotated in a sequence where one first rotate the cube with angle ϕ_1 then rotate with angle Φ and lastly rotate with angle ϕ_2. .

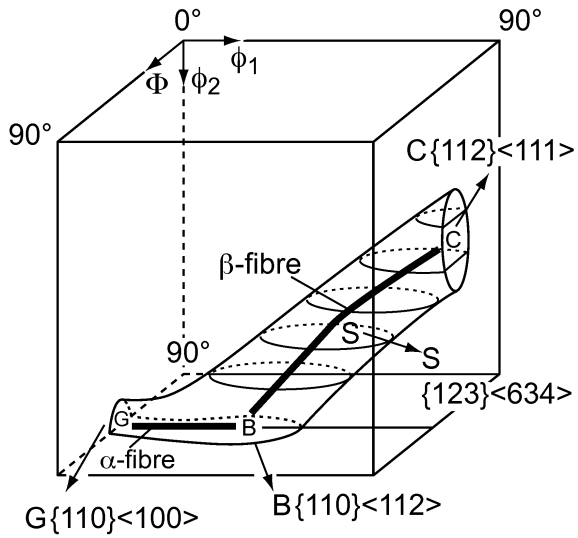

Figure 2.6: Euler space showing β-fibre(Goyal (2011))

The Euler angles corresponding to the texture of a sample can be represented in Euler space. Euler space is a three dimensional Cartesian plot where the axes is the three Euler angles. ϕ_1 and ϕ_2 goes from 0 to 360° and Φ goes from 0 to 180°. However in the case of cubic symmetry the range is reduced to 0-90°for all three angles, due to symmetry. A representation of Euler angles in Euler space for a material is called Orientation Distribution Function (ODF) as shown in Figure 2.6. An ODF is usually represented by showing a set of slices for different values of Φ as shown in Figure 2.7

2.4 Metal deformation

Metal deformation can be divided into elastic and plastic deformation. At smaller stresses and strains elastic deformation will dominate.

Plastic deformation of metals usually happens by slip or by twinning. In metals with high stacking fault energy, such as aluminium, deformation by slip is most common (Humphreys and Hatherly (2004). Slip is sliding of blocks of atoms along a defined crystallographic plane and a defined crystallographic direction (Dieter (2015). This plane

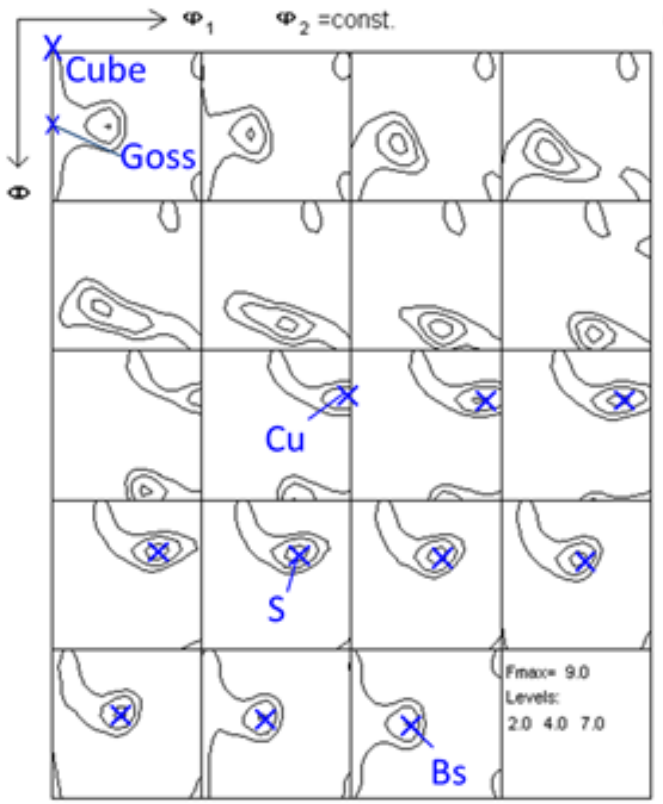

Figure 2.7: An ODF showing the placement of th Cube component, the Goss component and the components in the β-fibre.

is called a slip plane. The direction of the sliding is also a defined direction called slip direction, which lies in the slip plane. The slip plane is defined by the Miller indexes of a vector normal to the slip plane and the slip direction is categorised by its Miller indexes and its vector is called Burger's vector ($\mathbf{b}$). This sliding is called a slip and requires a critical resolved shear stress to be activated (CRSS). CRSS is the crystallographic equivalent of the macroscopic yield stress and depends on the composition of the material, the temperature and which slip system is activated. The critical resolved sear stress can be related to a macroscopic stress on a single crystal by the use of the Schmid factor ($\mathbf{q}$) shown in Equation 2.3.

$$\tau_{\mathbf{r}} = \sigma \cos\phi \cos\lambda = \mathbf{q}\sigma \tag{2.3}$$

Where $\tau_{\mathbf{r}}$ is the resolved shear stress and σ is the macroscopic stress. $\cos\phi\cos\lambda$ is the Schmid factor(q) and here ϕ and λ are the angles between σ and the slip plane and the angle between σ and the slip direction. The material will slip when the resolved shear stress is equal to the CRSS. From Equation 2.3 one can see that the resolved shear stress is maximum when $\phi = \lambda = 45°$. This means that a slip system having this orientation with

respect to the macroscopic strain will be activated easier than slip systems having different orientations. The Schmid tensor is given by Equation 2.4 where $\mathbf{n}^s$ is the normal vector of the slip plane and $\mathbf{s}^s$ is the vector of the slip direction.

$$q_{ij}^s = \frac{1}{2}(s_i^s n_j^s + s_j^s n_i^s) \tag{2.4}$$

Just slip is not enough for a grain to change from its start geometry to the macroscopic deformed geometry. This is demonstrated in Figure 2.8. Total deformation consists of both a slip part and a rotation part. It is the last part that leads to the evolution of certain texture. The grains tend to rotate towards a set of specific orientations, characteristic for the crystal structure and deformation mode.

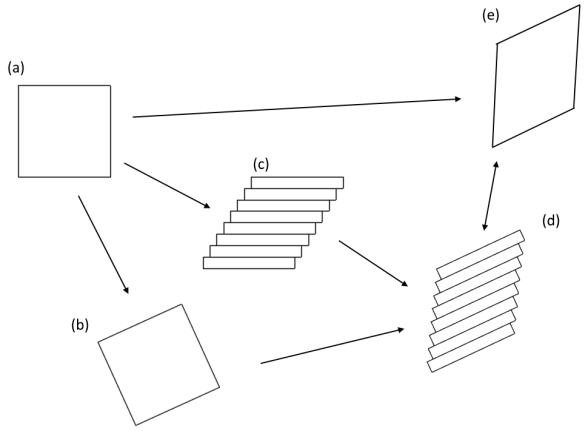

Figure 2.8: To deform a grain with a shape equal to (a) to shape equal to (e) the grain will both be deformed by slip((a) to (c)) and rotation ((a) to (b)). This gives the total deformation

The stress needed for deformation is dependent on the rate of strain. This dependence is called strain rate sensitivity. For uni-axial tensile deformation are the strain rate sensitivity given as Equation 2.5. For FCC metals are the strain rate sensitivity usually small at room temperature ($m \approx 1/100$ Gottstein (2004). AA6082 has $m = 0.064$ at 375°C and $m = 0.148$ at 515°C acording to Oosterkamp et al. (2000). Verlinden et al. (1993) found the strain rate sensitivity of AA6060 to be: 0.14 at 390°C, 0.15 420°C, 0.17 at 450°C, 0.19 at 480°C, 0.20 at 510°C and 0.22 at 540°C.

$$m = \frac{d \ln \sigma}{d \ln \dot{\epsilon}} \tag{2.5}$$

Some typical deformation modes are uni-axial tensile deformation and plane strain deformation. Uni-axial tensile deformation has a deformation gradient as given in Table 2.4. This deformation is a axisymmetric deformation. Because of the symmetry, a fibre texture is usually generated. Cold-drawn FCC metals generally has $\langle 100 \rangle$-fibre and $\langle 111 \rangle$-fibre texture, where most grains have a $\langle 100 \rangle$-direction or a $\langle 111 \rangle$-direction parallel to

Table 2.4: Velocity gradients of uni-axial tensile deformation.

Velocity gradient		
1	0	0
0	-0.5	0
0	0	-0.5

Table 2.5: Velocity gradients of plane strain deformation.

Velocity gradient		
1	0	0
0	0	0
0	0	-1

the drawing direction(Verlinden and Cahn (2007). Plane strain is deformation as given in Table 2.5. This deformation usually leads to a texture containing α-fibre and β-fibre.

2.4.1 Slip systems in aluminium

The crystal structure of aluminium is FCC. This means the close packed planes are the $\{111\}$ planes and the close packed directions are the $\langle 110 \rangle$ directions. There are 4 unique $\{111\}$ planes and each of them contains 3 $\langle 110 \rangle$ directions. This gives a total of 12 unique $\{111\}\langle 110 \rangle$ slip systems (Dieter (2015). At higher temperatures there are also observed slip on other slip systems than $\{111\}\langle 110 \rangle$, in so called non octahedral slip planes(Caillard and Martin (2009). These are $\{110\}\langle 110 \rangle$(Hazif and Poirer (1975), $\{100\}\langle 110 \rangle$(Beevers and Honeycombe (1961) and$\{112\}\langle 110 \rangle$(Couret and Caillard (1988).

2.4.2 Textures in aluminium

Deformation texture after plane strain deformation usually consist of β-fibre and α-fibre (Figure 2.6). The β-fibre consist of Copper $\{112\}\langle 111 \rangle$, S $\{123\}\langle 634 \rangle$ and Brass $\{011\}\langle 211 \rangle$. The α-fibre contain Brass along with Goss $\{011\}\langle 100 \rangle$.

Recrystallisation texture usually consist of Cube $\{100\}\langle 100 \rangle$, Goss $\{011\}\langle 100 \rangle$, P $\{011\}\langle 122 \rangle$ and Q $\{013\}\langle 231 \rangle$ texture components(Duckham et al. (2002), Engler (2003), Azari et al. (2004).

The location of the different texture components are shown in Figure 2.7.

2.5 Recrystallisation

Recrystallisation is the process where new grains are formed to replace old deformed grains. The recrystallisation process is usually divided into a nucleation phase and a growth phase. These processes are similar to nucleation and growth processes in solidification and in solid state phase transformations, but there are significant differences. One of these are that there is no "classical" nucleation because the driving force is much smaller than in the other nucleation processes. In "classical" nucleation the nucleate emerges as a

result of random atomistic fluctations leading to the formation of a small crystallite that can grow (Humphreys and Hatherly (2004). Nucleation of recrystallisation are small volumes, recovered sub- or cells, pre-existing in deformed microstructure, so-called deformation heterogeneities which fulfill the conditions for growth(Figure 2.9). An important consequence of this idea is that the orientation of each new grain arises from the same deformed state (Doherty et al. (1997).

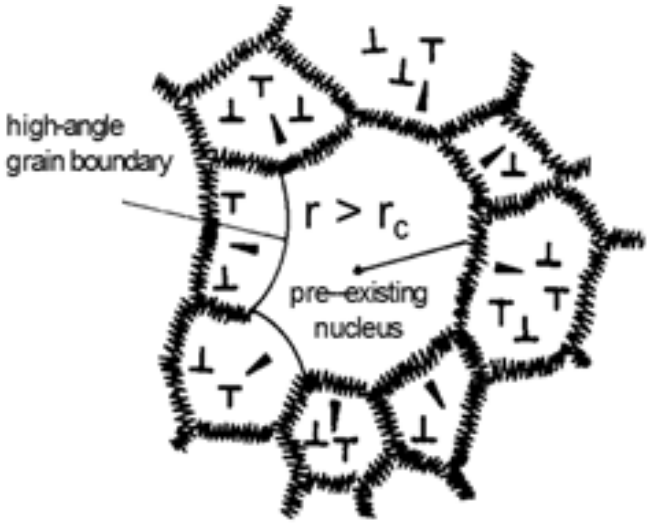

Figure 2.9: An illustration of a recrystallisation nucleus with growth potential (Gottstein (2004).

According to Burke and Turnbull the laws of recrystallisation is the following(Burke and Turnbull (1952) p. 222):

1. *A minimum deformation is necessary to cause recrystallisation*
2. *The smaller the degree of deformation, the higher is the temperature required to cause recrystallisation*
3. *Increasing the annealing time decreases the temperature necessary for recrystallisation*
4. *The final grain size depends chiefly upon the degree of deformation, and to a lesser extent on the annealing temperature, being smaller the greater the degree of deformation and the lower the annealing temperature*
5. *The larger the original grain size, the greater is the amount of cold deformation required to give equivalent recrystallisation temperature and time*
6. *The amount of cold work required to give equivalent deformational hardening increases with increasing temperature of working*

7. *Continued heating after recrystallisation is complete causes the grain size to increase.*

These laws are a bit outdated and more recent research has shown that recrystallisation is a more complex process than Burke and Turnbull envisioned. But these laws do still provide a useful guide about recrystallisation (Humphreys and Hatherly (2004). For instances it is demonstrated that large deformations gives a different recrystallisation behavior than low deformation.

The definition of a recrystallisation nucleus is: A Crystal of low internal energy growing into deformed or recovered material from which it is separated by a high angle grain boundary (Humphreys and Hatherly (2004). It is hard to detect and pinpoint a recrystallisation nucleus. Typical nucleation sites in aluminium are old grain boundaries, shear bands and deformation zones around non deformable particles(i.e. particle stimulated nucleation(PSN). Shear bands is bands, cutting across multiple grains, having high shear strain. The formation of these bands is strong in low-SFE metals and alloys (Verlinden and Cahn (2007). These bands are often orientation sensitive and can give nucleation of recrystallisation. Particle stimulated nucleation is nucleation in the deformed zone around non-deformable particles. Recrystallisation texture from PSN are evidently shown to be generally weak and contains ND-rotated cube components and P components at deformations above 90% (Engler et al. (1997).

Cube bands and Cube oriented grains that survived plane strain rolling are proven to be nucleation points for Cube recrystallisation texture in cobber (Hong and Lee (2003). In aluminium are the nucleation points shear bands located in ND-rotated Cube grains and Copper texture components (Hjelen et al. (1991).

Growth of high angle grain boundaries into the deformed structure is the main growth mechanism for recrystallised grains. The difference between growth of high angle boundaries and low angle boundaries is 100 - 1000 times in favour of high angle boundaries (Doherty et al. (1997). Research have proven that a misorientation angle of about 40°between the recrystallised grain and the deformed structure gives the highest mobility (Lücke et al. (1976).

Conditions that promote recrystallisation could be divided into size advantage and frequency advantage. Frequency advantage are conditions that promotes nucleation. This is typically large variations in stored energy. Size advantage comes from conditions that promotes growth of certain recrystallised grains. An example that can lead to size advantage is early nucleation. Zener drag from particles can lead to a size disadvantage (Verlinden and Cahn (2007).

Zener drag also called particle pinning is the effect dispersed particles has on the movement of high angle grain boundaries. The Zener drag can be used effectively to control the grain size in a particle-containing alloy (Verlinden and Cahn (2007). The pinning pressure is given in equation 2.6 where F_v is particle volume fraction, γ is grain boundary energy and r is the particle size. As we see a large pinning pressure is favored by a high volume fraction of small particles.

$$P = \frac{3F_v\gamma}{2r} \tag{2.6}$$

2.6 Crystal plasticity modelling

Crystal plasticity modelling can be used to simulate flow-stress and texture development during deformation of a metal. In this thesis ALAMEL and VPSC simulation software are used to predict deformation texture. Two classical models used for simulation of deformation texture are the upper bound Taylor model and the lower bound Sachs model. All of these models/simulation softwares will be discussed here.

2.6.1 Taylor model

Basic for most deformation texture modeling tools is that they build on the Taylor model. Central for this type of modelling is that each grain in a poly crystal will experience the same strain as the macroscopic strain.

Both the Taylor model and the Sachs model (discussed later) incorporates the different slip systems of each grains by the use of the Schmid factor. Their input are the statistical distribution of orientations of all grains in the material before deformation. During the modeling the grain orientations will be updated for each step dependant on how much each grain is rotated. For the Taylor model each grain is rotated and deformed, to the applied deformation, in a way so that the total deformation work rate is minimised as given by Equation 2.7 (Hirsch and Lücke (1988). Here is $\dot{U}$ the work rate, τ_0^s the stress needed to activate a slip system and $\dot{\gamma^s}$ is the rate of shear deformation (the absolute of $\dot{\gamma^s}$ is used in the minimisation of work). This is equal to Equation 2.8 if one assumes that τ_0^s is equal for all slip system. s denotes in this equation the slip system so the energy used are the sum of energy used in each slip system.

$$\dot{U} = \sum_s \tau_0^s \dot{\gamma^s} \tag{2.7}$$

$$\dot{U} = \sum_s \dot{\gamma^s} \tag{2.8}$$

The relationship, between shear strain for a slip system (γ^s) and total deformation and the strain tensor for a slip system ($\mathbf{E}^s$), is given by Equation 2.9. Minimisation of $\dot{\gamma^s}$ yields the same results as minimisation of γ since the macroscopic strain rate is constant. Since the deformation of grain is the sum of slip deformation and rotation, the strain tensor is given by Equation 2.10 where $\mathbf{\Omega}$ is the grain rotation. Deformation by slip is the symmetric part of the deformation tensor and grain rotation is the anti-symmetrical part of the deformation tensor. This means that the relation between $\mathbf{L}$ (the displacement gradient tensor) and $\mathbf{E}^s$ can be given by Equation 2.11 where t means the transpose of a matrix. This leads to Equation 2.12, which is used together with the minimisation of γ to get the activated slip systems. The rotation of the grain is then obtained by putting the results into the antisymmetric part of the equation (Equation 2.13).

$$E_{ij}^s = n_j^s v_i^s \gamma^s \tag{2.9}$$

$$\mathbf{L} = \sum_s \mathbf{E}^s + \mathbf{\Omega} \tag{2.10}$$

$$\frac{1}{2}(\mathbf{L}+\mathbf{L}^t)=\frac{1}{2}\sum_s(\mathbf{E}^s+\mathbf{E}^{ts}) \tag{2.11}$$

$$\frac{1}{2}(\mathbf{L}+\mathbf{L}^t)=\frac{1}{2}\sum_s(n_j^s v_i^s+n_i^s v_j^s)\gamma^s \tag{2.12}$$

$$\frac{1}{2}(\mathbf{L}-\mathbf{L}^t)=\frac{1}{2}\sum_s(n_j^s v_i^s-n_i^s v_j^s)\gamma^s+\Omega_{ij} \tag{2.13}$$

The FC-Taylor model has shown to give good predictions of the orientation of the β-fibre for rolled samples, but does not correctly predict the different densities along this fibre (Hirsch and Lücke (1988).

2.6.2 Sachs model

The Sachs model is similar to the Taylor model in that both are a statistical approach to crystal plasticity simulation. The Sachs model differs from the Taylor model in that it has equal stress for all grains instead of equal strain. For the Sachs model the activated slip system is the slip system having the highest resolved Schmid factor. Slip deformation can be calculated by just using the slip on the active slip system as in Equation 2.12 and rotation can be calculated the same way as done in the Taylor model. While the Taylor model may be denoted an "iso-strain" model, the Sachs model is an "iso-stress" model. Due to the strain incapability that develops the Sachs model is usually only applicable at small strains

2.6.3 ALAMEL

ALAMEL is a Taylor-type model for modeling textures. It differs from the Taylor model because it also considers influences between grains. It does so by creating pairs of two and two grains where the pair has the same deformation as the macroscopic deformation but each of them can have a deformation that differ from the macroscopic deformation.

The ALAMEL model allows for the use of different relaxations. In the case of no relaxation the ALAMEL model is identical to the full constraint model (FC-Taylor). In this case that each grain has the same deformation. While a full constraint model (FC-Taylor) has the same macroscopic deformation as the local deformation for all grains, the relaxed model has one or more elements in the local deformation matrix which does not need to be the same as in the macroscopic deformation matrix. Sachs model is a Relaxed constraint model where there are full relaxation.

For classical relaxation models the relaxation are done by choosing two grain orientations at random which is coupled together with a relaxed shear stress between each other. In the ALAMEL model this is done by connecting a grain to several other by the grain boundaries. The areas close to the grain boundaries are influenced by the areas at the other side of the grain boundary. This is shown in Figure 2.10. The rest of the grain is deformed and rotated as in Taylor model.

Different relaxations in ALAMEL are shown in Figure 2.11. Type I is relaxation of L_{13} shear, Type II is relaxation of L_{23} shear and Type III is relaxation of L_{12} shear (Mánik

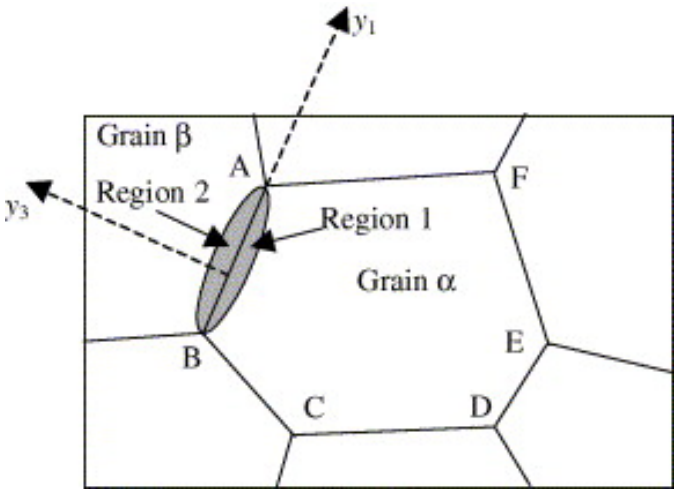

Figure 2.10: The areas close to the grain boundaries are influenced by the other grain(Houtte et al. (2005).

and Holmedal (2013). As seen from this figure two coupled grains have opposite shear deformation for Type I and Type II, but the shear is equal for both grains in Type III.

The strain of each grain is as given by Equation 2.14 for one grain and Equation 2.15 for the other grain in a pair. The relaxation shear is added to the minimisation of work rate as given in Equation 2.16 where RLX means that it is the relaxation part.

$$\epsilon_{\mathbf{1}} = \mathbf{E} - \sum \mathbf{K}\dot{\gamma}^{RLX} \tag{2.14}$$

$$\epsilon_{\mathbf{2}} = \mathbf{E} + \sum \mathbf{K}\dot{\gamma}^{RLX} \tag{2.15}$$

$$\dot{U} = \sum_{G} \left(\sum_{s} \tau_{G}^{s} |\gamma_{G}^{s}| + \sum_{r} \tau_{rG}^{RIX} |\gamma_{rG}^{RIX}| \right) \tag{2.16}$$

2.6.4 VPSC

VPSC stands for Viscoplastic Self Consistent. Self Consistent refers to the approach used in this model. This means that each grain is represented as a homogeneous inclusion in a homogeneous medium. The medium is the effective average of all grains in a polycrystal. The medium will influence the grains with and interaction equation. VPSC differs from the Taylor model because the individual grains do not need to have the same deformation as the macroscopic deformation. As with classical Taylor-model the grains are represented by their orientation and volume fraction. The VPSC model is explained by the creators in Lebensohn and Tomé (1993).

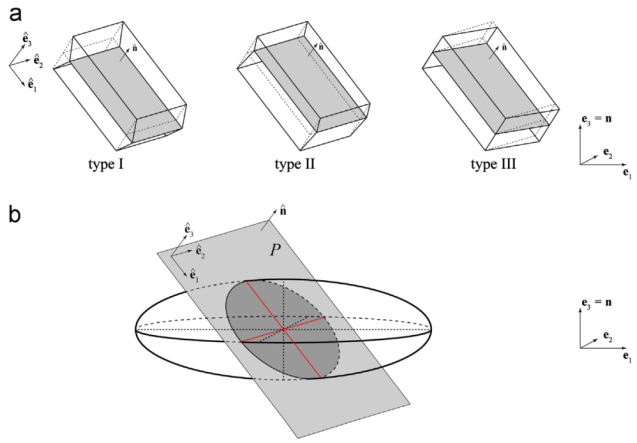

Figure 2.11: (a) Different relaxation (b) Intersection plane in an ellipsoid grain(Mánik and Holmedal (2013).

The medium has strain rate $\dot{\mathbf{E}}$ and a compliance matrix $\overline{\mathbf{M}}$. Each grain((r)) also has a strain rate $\dot{\epsilon}^{\mathbf{0}}$ and a compliance matrix $\mathbf{M^{(r)}}$. The compliance matrix describes the relationship between the stress and the strain given as:

$$\epsilon_{ij}^{(r)} = M_{ijkl}^{(r)}\sigma_{kl}^{(r)} + \epsilon_{ij}^{0(r)} \tag{2.17}$$

$$E_{ij} = \overline{M}_{ijkl}\Sigma_{kl} + E_{ij}^{0} \tag{2.18}$$

Here are σ the stress in a grain and Σ is the stress for the medium. How to find $\mathbf{M^{(r)}}$ is dependent on which form of linearisation is used. This will be discussed later in this chapter. For these equations and most other equations in this chapter Einstein notation for summation is used.

Finding $\mathbf{E}$ could be done by using $E_{ij} = \langle\epsilon_{ij}^{(r)}\rangle$. Where "$\langle\rangle$" means the weighted average of all grains weighted by volume fraction.

Two different approaches to finding $\mathbf{M^{(r)}}$ where used in this work. The secant, noted as sec, method is given in Equation 2.19. Here τ_0 is the shear stress required for slip, γ_0 the shear strain of a slip, $\sigma^{(r)}$ the stress in the grain and $\mathbf{q^s}$ the Schmid factors. The second method is called tangent(tan) and the relationship between tan and sec is given by Equation 2.20 where n is the reciprocal of the strain rate sensitivity ($n = 1/m$). This rate sensitivity is possible to vary during simulation and two different rate sensitivities are used in this project.

$$\mathbf{M_{ijkl}^{(r),sec}} = \gamma_0 \sum_s \frac{q_{ij}^s q_{kl}^s}{\tau_0^s} \left(\frac{q_{pq}^s \sigma_{pq}^{(r)}}{\tau_0^s} \right)^{n-1} \tag{2.19}$$

$$\overline{M}^{tan} = n\overline{M}^{sec} \tag{2.20}$$

The tangent and secant interaction scheme between strain rate and stress are represented in Figure 2.12. Here are $\overline{D}$ strain rate and $\overline{\sigma}$ stress. When $n \to \infty$ ($m \to 0$)

the tangent scheme approaches a lower bound model (Sachs) and the secant scheme approaches an upper bound model (Taylor) (Lebensohn and Tomé (1993). This can also be seen in Figure 2.12.

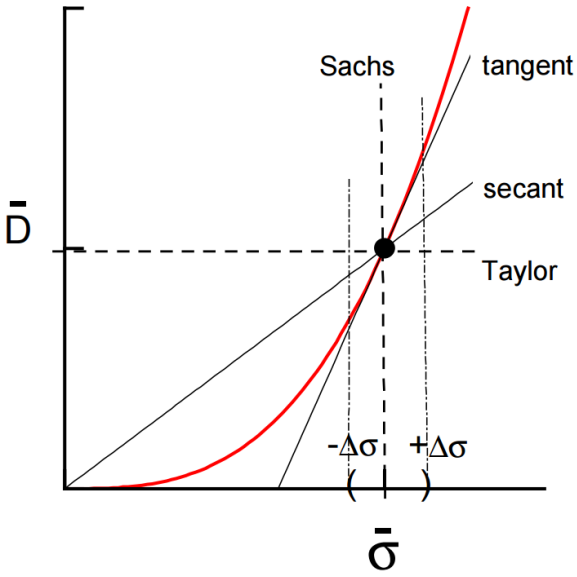

Figure 2.12: One-dimensional representation of the relationship between stress and strain rate using tangent and secant interaction (Tomé (1999).

The Schmid factors $\mathbf{q^s}$ are related to the different slip systems, which is noted by an s. This is found by using Equation 2.4. Where $\mathbf{n}$ and $\mathbf{s}$ correspond to one slip system in one grain with a certain orientation.

Each step is done by finding the solution of Equation 2.21 where $\tilde{\mathbf{M}}$ is the interaction between the deviation strain($\tilde{\epsilon}$) and deviation stress($\tilde{\sigma}$) as in equation 2.22. $\tilde{\mathbf{M}}$ is obtained by using the Eshelby tensor (Equation 2.23).

$$\gamma_0 \sum_s \left(\frac{q^s_{pq} \sigma^{(r)}_{pq}}{\tau^s_0} \right)^n - E_{ij} = -\tilde{M}_{ijkl}(\sigma^{(r)}_{kl} - \Sigma_{kl}) \tag{2.21}$$

$$\tilde{\epsilon}^{(r)}_{ij} = -\tilde{M}_(ijkl)\tilde{\sigma}^{(r)}_{ij} \tag{2.22}$$

$$\tilde{M}_(ijkl) = (I - S)^{-1}_{ijmn} S_{mnpq} \overline{M}_{pqkl} \tag{2.23}$$

Chapter 3

Materials and Methods

This chapter is divided into an experimental part and a simulation part. The experiments is done using extruded aluminium rods of alloy AA6060 and AA6082 (having a diameter of 20 mm) and an extruded flat profile of AA6082 (having a thickness of 10 mm). The extruded rods are examined as extruded cylindrical rod, after subsequent rolling and after annealing of the rolled profiles material. The samples are examined by EBSD in SEM and by XRD. The simulations were carried out by using the VPSC software and the ALAMEL software. The simulations were done with uni-axial tensile deformation and plane strain deformation.

3.1 Material

For this report aluminium AA6082 and AA6060 were used. The AA6082 extruded flat profile was received from Ph.D. student Zebing Xu. This material was extruded at Hydro. Both the AA6060 and the AA6082 alloys were extruded into cylindrical rods by the SINTEF press.

The flat profile was extruded Hydro. The billet was homogenised at 580°C for 3 hours. the extrusion was performed at 500°C having an extrusion ratio of 12 making the average strain 2.5. The profile had a thickness of 10 mm and a width of 80 mm.

The cylindrical rods, extruded at the SINTEF press, were extruded from an initial billet radius of 95 mm into cylindrical rods having a diameter of 20 mm. This gives a true strain elongation of 3.1. The temperature during these extrusion were believed to be about 500°C according to standard extrusion procedures for these alloys at the SINTEF press. However as we do not have access to the exact extrusion parameters a certain uncertainty exists with respect to the actual extrusion parameters for these materials.

3.1.1 Rolling

A 8 mm thick plate was cut out from the centre of the extruded rod so that the thinnest direction is in the transverse direction of the cylinder. This is illustrated in Figure 3.1. The

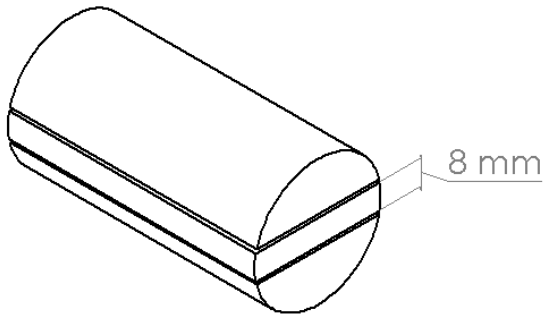

Figure 3.1: The plate was cut out of the rod as shown in this picture

Table 3.1: Parameters for electropolishing

Parameter	value
Time	20 s
Flow rate	8
Temperature	-30 °C
Voltage	31 V

AA6082-plate was rolled to a thickness of 3 mm and 2 mm, respectably, through several passes at a low speed. The AA6060-plate was rolled to a thickness of respectively 2.7 mm and 2 mm.

3.1.2 Annealing

The samples were annealed after rolling. The annealing was carried out in a salt bath at the temperatures 450°C and 550°C. The samples were heated for 100 s for both temperatures and quenched right after annealing. The 2 mm thick rolled AA6060 plate annealed at 450°C was further annealed for 10 minutes in addition to the 100 s.

3.2 EBSD

3.2.1 Surface preparation

The sample was prepared for EBSD by the use of grinding, polishing and electropolishing. The electropolishing was carried out with the help of a Struers LectroPol-5 and the parameters used are given in table 3.1.

3.2.2 Data Collection

The EBSD measurements were done with a FESEM Zeis Ultra 55. The resulting data was analysed with OIM Data Collector and OIM Data Analysis. For both the rolled and the

Table 3.2: Velocity gradients with modified plane strain deformation.

Velocity gradient		
1	0	0
0	-0.2	0
0	0	-0.8

unrolled samples the pictures were taken in the ED-TD plane close to the centre for both the cylindrical extrusion rod and the rolled samples.

3.3 X-Ray Diffraction

3.3.1 Surface preparation

The RD-TD-direction of the rolled sample was grinded to the centre plane. Then it was grinded with 2400 mesh grinding paper. The sample was etched in a 10-20% NaOH solution containing one teaspoon of sugar per liter solution for 10 minutes. It was thereafter dipped in water before being etched in 20-30% HNO_3 for 20-30 seconds.

3.3.2 Data Collection

The X-ray difraction was done by a Siemens D5000 X-ray diffractometer. The sampling was done in the RD-TD direction.

3.4 Simulation of deformation texture

The simulation of deformation texture were carried out having different deformation modes. The first simulations were done using uni-axial tensile deformation. The velocity gradients matrix for this deformation is given in Table 2.4. In these simulations the starting texture was a random texture.

The second part of the simulation were done with plane strain deformation. The corresponding velocity gradient matrix is given in Table 2.5. The input texture in these simulations were a $\langle 111 \rangle$-fibre texture or a $\langle 100 \rangle$-fibre texture. These simulations were carried out at varying true strain from 0.8 to 2. Each simulation had 100 steps were each increment was equal to the total deformation divided by 100. Another set of simulations were done for the same input fibres and the velocity gradient given in Table 3.2. This deformation velocity gradient matrix is called modified plane strain in this thesis. These simulations were preformed with a true strain of 2.

3.4.1 VPSC

The deformation textures were simulated using VPSC. Different simulations were done by activating different slip systems and by applying different values of the parameter rate sensitivity (Equation 2.19). The activated slip systems are divided into five different sets

Table 3.3: The sets of slip systems used in this simulation.

Name	Activated slip systems
I	$\{111\}\langle 110\rangle\, \tau_0 = 1$
II	$\{111\}\langle 110\rangle\, \tau_0 = 1 + \{100\}\langle 110\rangle\, \tau_0 = 0.5$
III	$\{111\}\langle 110\rangle\, \tau_0 = 1 + \{112\}\langle 110\rangle\, \tau_0 = 0.5$
IV	$\{111\}\langle 110\rangle\, \tau_0 = 1 + \{110\}\langle 110\rangle\, \tau_0 = 0.5$
V	$\{111\}\langle 110\rangle\, \tau_0 = 1 + \{100\}\langle 110\rangle\, \tau_0 = 1$ $+\{112\}\langle 110\rangle\, \tau_0 = 1 + \{110\}\langle 110\rangle\, \tau_0 = 1$

which are named I to V. These are given in Table 3.3. τ_0 is the CRSS. The non-close packed slip systems, added to the simulations, had a lower activation stress for slip than the close packed slip systems. This was done so that it is easier to recognise the effect the addition of a slip system has on the texture. Each of these was used having strain rate sensitivity of both $m = 0.2$ and $m = 0.05$. For sets II, III and IV the slip system which is not $\{111\}\langle 110\rangle$ had an activation stress(τ_0) of 0.5 compared to 1 for $\{111\}\langle 110\rangle$.

3.4.2 ALAMEL

The deformation texture was also simulated by using the ALAMEL model. The set of activated slip systems used in these simulations were equal to those used in VPSC (Table 3.3). Simulations were also carried out by using different constraints and relaxations on the shear plane. These sets were FC-Taylor, ALAMEL and ALAMEL-type III.

Chapter 4

Results

4.1 Experimental

The experimental work was carried out on AA6082 and AA6060. An AA6082 sample was extruded into a flat profile at high temperatures. Both an AA6082 sample and an AA6060 sample were extruded to a cylindrical rod and subsequently rolled. The material was recived in their extruded state. The billet for the AA6082 extruded flat profile was DC-casted and homogenised at 580°C for 3 hours. The extrusion was performed at 500°C with an extrusion ration of 12 making th average accumulate strain $\sim$2.5. The cylindrical rods of both AA6082 and AA6060 are both assumed to have the same extrusion conditions although exact information is not available.

The motivation of the experimental work was firstly to provide typical microstructures and textures for extrusion of flat profiles and cylindrical rods. AA6082 has deformed (non-recrystallised) microstructure trough all forming steps thus producing a reference texture for high temperature deformation. Secondly is the motivations based on the fact that the centre of a extruded flat profile experiences uni-axial deformation in the container and plane strain near and in the pocket. This is shown in Chapter 4.2.1.

The experimental are presented in 4 section. First are the extruded flat profile presented (Chapter 4.1.1), then the extruded cylindrical rods are presented (Chapter 4.1.2). The extruded cylindrical rod material are rolled at cold temperatures. The resulting microstructures and textures are presented in Chapter 4.1.3 The rolled profiles were annealed at two different temperatures. This was done to to see what microstructure and texture the recrystallised material has and to see if there are any differences in texture and microstructure with different annealing temperatures. This is presented in Chapter 4.1.4.

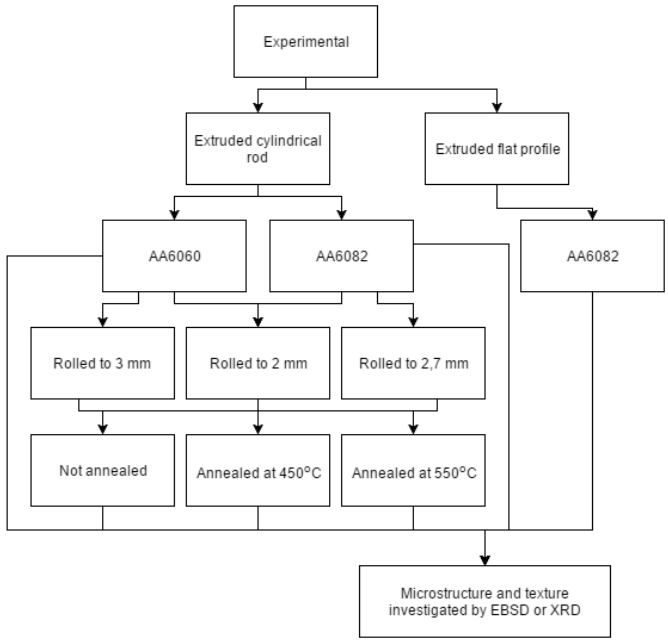

Figure 4.1: Flowchart describing the different experimental results obtained.

The flowchart in Figure 4.1 shows the different samples investigated in this report. The microstructures and textures, obtained by the use of EBSD and XRD, are presented in this section. The microstructure is represented by micrographs and the texture are represented by ODFs and pole figures. EBSD was done on the ED-TD-plane for extruded cylindrical profile and on the ED-ND-plane for the extruded flat profiles and the rolled samples. The XRD was done on the ED-TD-plane for the rolled samples.

4.1.1 Extruded flat profile

The extruded flat profile is of AA6082. The profile has thickness of 10 mm and a width of 80 mm. The extrusion was carried out at hydro and performed at a temperature of about 500°C and extrusion ratio of 12.

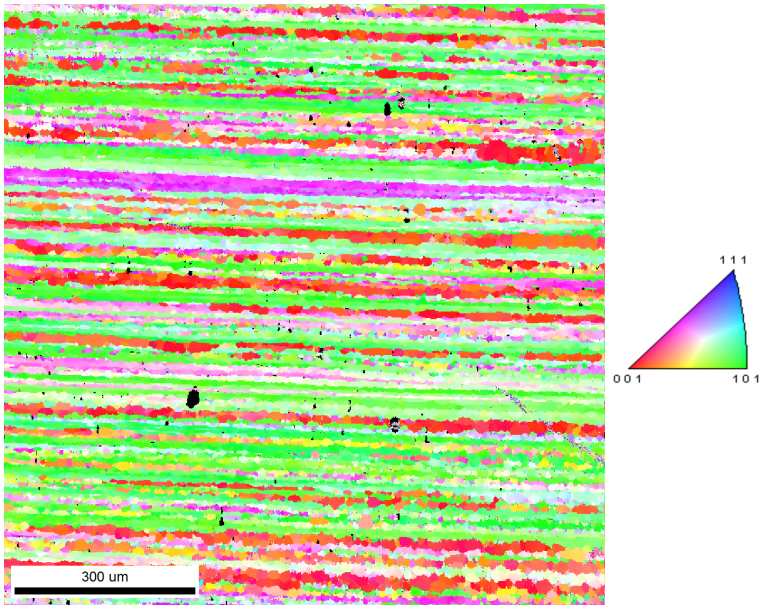

Figure 4.2: IPF-micrograph of the centre of an extruded flat profile of AA6082 with a thickness of 10 mm.

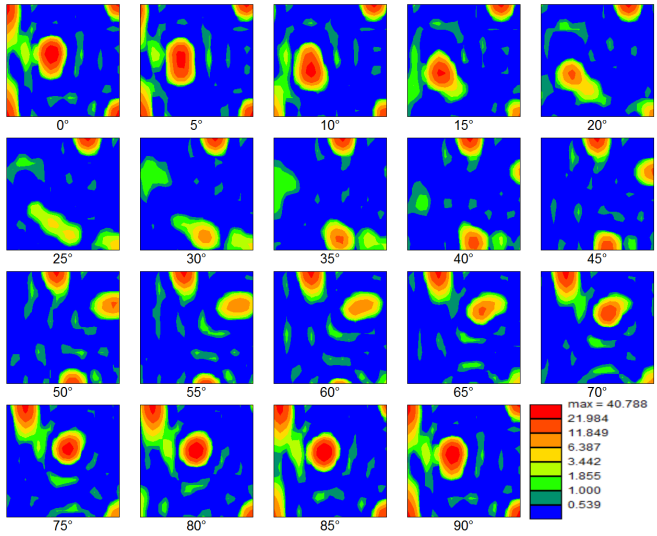

Figure 4.3: ODF of the centre of an extruded flat AA6082 profile with a thickness of 10 mm.

Figure 4.2 and Figure 4.3 show the IPF mapping and the ODF for the centre of an extruded flat profile for the alloy AA6082. The IPF mapping show a deformed/unrecrystallised microstructure. The resulting texture for this deformation is the typical β-fibre and Cube

component. The Cube component has a peak of around 25 times random, the β-fibre has the highest intensity at the Brass component where the intensity is around 40 times random. The Cu component has an intensity of around 13 times random and the S component has an intensity of 10 times random.

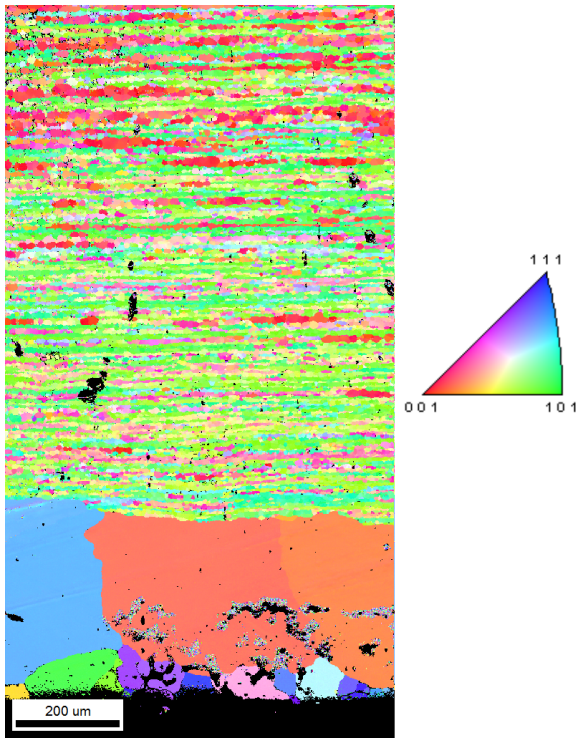

Figure 4.4: IPF-micrograph taken near the surface of an extruded flat profile of AA6082 with a thickness of 10 mm.

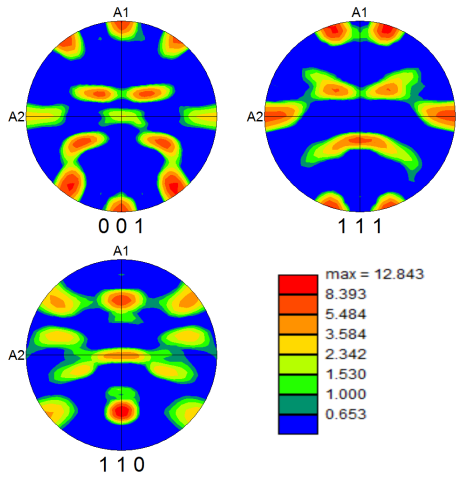

Figure 4.5: pole figure of area close to the surface of an extruded flat AA6082 profile with a thickness of 10 mm. The recrystallised grains near the surface are not used to calculate this pole figure

Figure 4.4 shows an IPF-micrograph of the area close to the surface in the AA6082 extruded flat profile. The IPF-micrograph shows large recrystallised grains near the surface and a deformed microstructure further from the surface. Figure 4.5 shows a pole figure of the deformed texture. The large recrystallised grains are not used in the calculation of this pole figure. The pole figure shows a unsymmetrical texture. The texture contains beta fibre and Cube components.

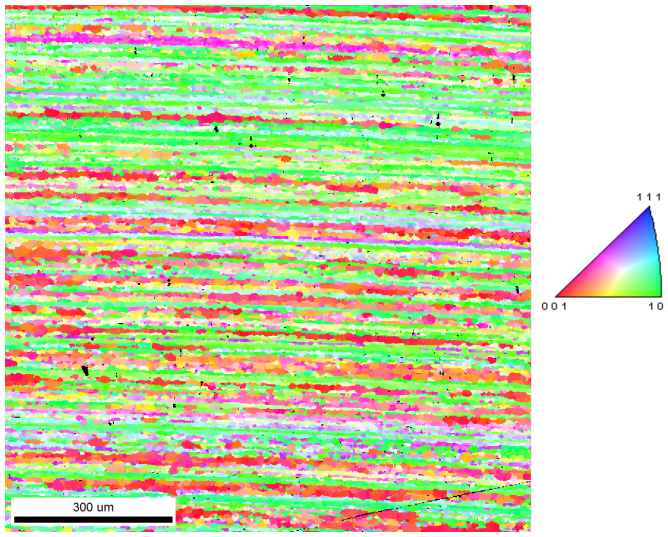

Figure 4.6: IPF-micrograph of an area going from 1.5 mm from the surface to 2.5 mm from the surface in an extruded flat profile of AA6082 with a thickness of 10 mm.

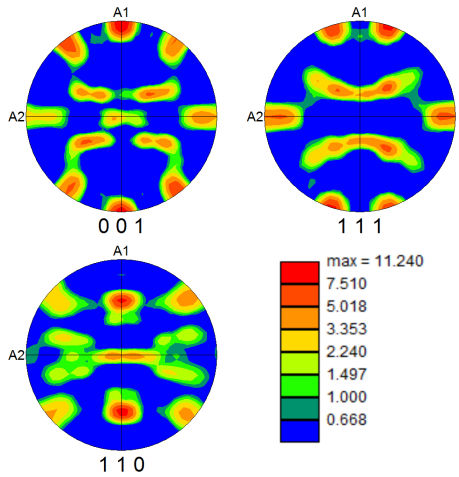

Figure 4.7: pole figure of an area going from 1.5 mm from the surface to 2.5 mm from the surface of an extruded flat AA6082 profile with a thickness of 10 mm.

Figure 4.6 shows the IPF-micrograph of the are between the area presented in Figure 4.2 and Figure 4.4. The IPF shows a deformed microstructure. The texture of this area is symmetrical. It shows the β-fibre and Cube components. The texture is close to the texture in the centre of the sample.

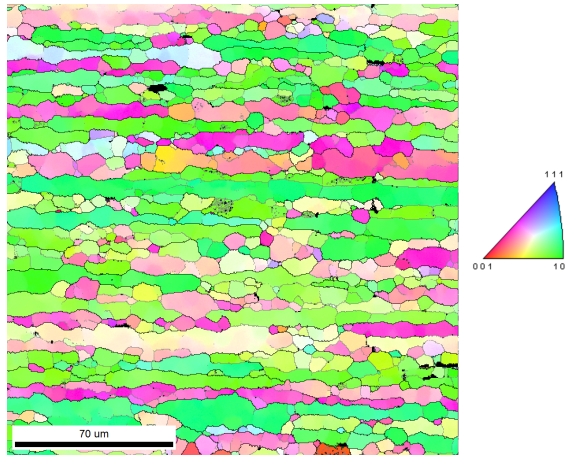

Figure 4.8: IPF-micrograph of an area 0.5 mm from the surface of the extruded flat profile of AA6082 with a thickness of 10 mm.

Figure 4.8 shows an IPF-micrograph of an area 0.5 mm from the surface of the extruded flat profile of AA6082. This area has a subgrain size of 6.0 ± 3.2 μm.

4.1.2 Extrusion of cylindrical profiles

AA6082 material

This experiment refers to extrusion of AA6082 cylindrical rod. The extrusion were done by the SINTEF press. The rod has a diameter of 20 mm from a assumed starting diameter of 95 mm. It is assumed that the extrusion temperature were 500°C. The average elongation of this material during extrusion is calculated to 3.1.

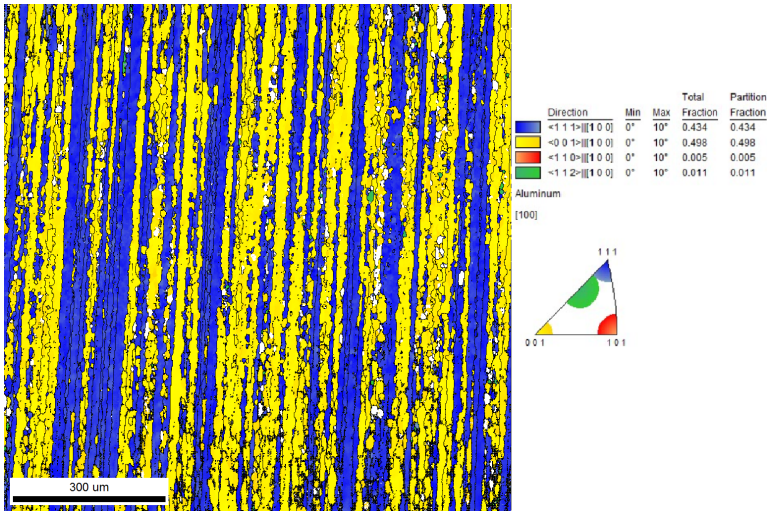

Figure 4.9: EBSD orientation map of the centre of an extruded AA6082 rod.

Figure 4.9 shows a EBSD-micrograph of the extruded AA6082 rod where different fibres are marked with different colors. This is clearly a fibrous structure. The EBSD-image shows that $\langle 111 \rangle$- and $\langle 100 \rangle$-fibres are the dominating fibres after plane stress deformation. $\langle 111 \rangle$-fibre and the $\langle 100 \rangle$-fibres have a volume fraction of 0.43 and 0.50 respectably. These measurements span across 10°from the measured fibre-directions. As seen from the ODF, in Figure 4.10, the texture is quite sharp and both the $\langle 111 \rangle$-fibre and the $\langle 100 \rangle$-fibre has even intensity along the fibres. The fibres can also be seen in the Pole figures (Figure 4.11).

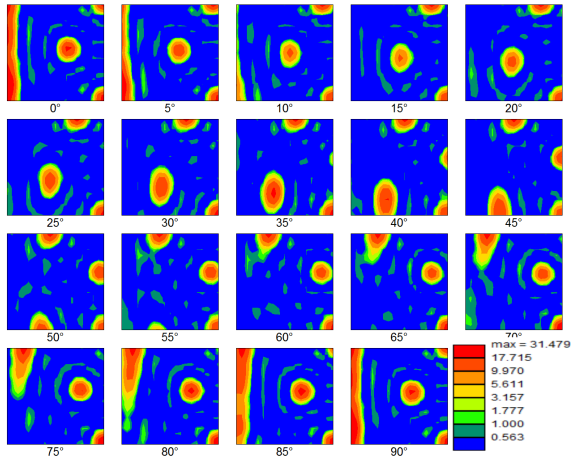

Figure 4.10: ODF from the centre of AA6082 extruded cylindrical rod.

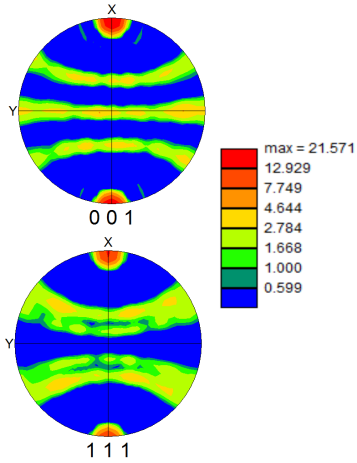

Figure 4.11: Pole figures from the centre of AA6082 extruded cylindrical rod.

AA6060 material

The extrusion of AA6060 cylindrical rod were also done at the SINTEF press. The rod has a diameter of 20 mm from a assumed starting diameter of 95 mm. It is assumed that the extrusion temperature were 500°C. The average elongation of this material during extrusion is calculated to 3.1.

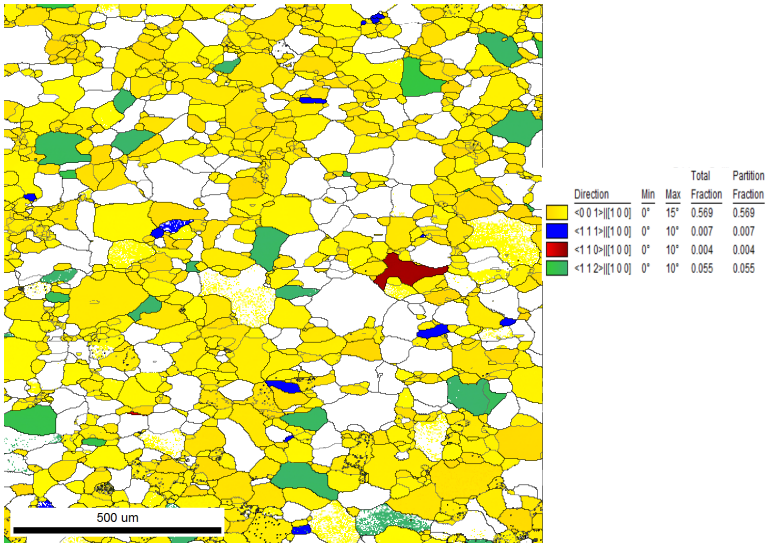

Figure 4.12: EBSD orientation map from the centre of an extruded AA6060 rod.

Figure 4.12 shows an EBSD-orientation map of the extruded AA6060 rod. Here we see that almost 0.6 of the sample has a $\langle 100 \rangle$-direction parallel to the ED-direction. This can also be recognised in the ODF in Figure 4.13 where one also can see that the $\langle 100 \rangle$-fibre is not as sharp as the $\langle 100 \rangle$-fibre in the AA6082 rod. The rest of the grains have random orientation. The EBSD-map also shows that the rod is recrystallised. The $\langle 100 \rangle$-fibre can bee seen in the Pole figures in Figure (4.14)

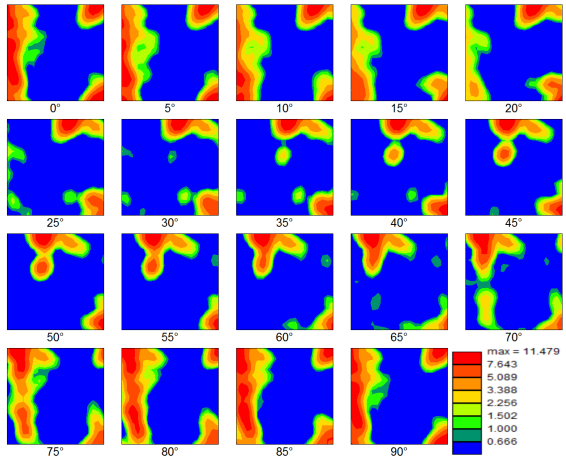

Figure 4.13: ODF from the centre of AA6060 extruded cylindrical rod.

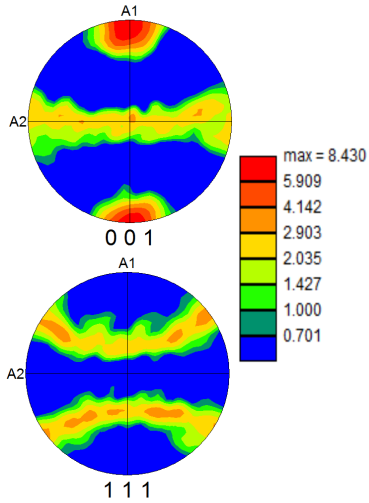

Figure 4.14: Pole figures from the centre of AA6060 extruded cylindrical rod.

4.1.3 Rolling of extruded round profile material

AA6082 material

In this experiment 8 mm thick section was cut out of the extruded of AA6082 round profile and rolled to 3 mm and 2 mm. The rolling were carried out at room temperature. The data were taken from the centre of the rolled plates.

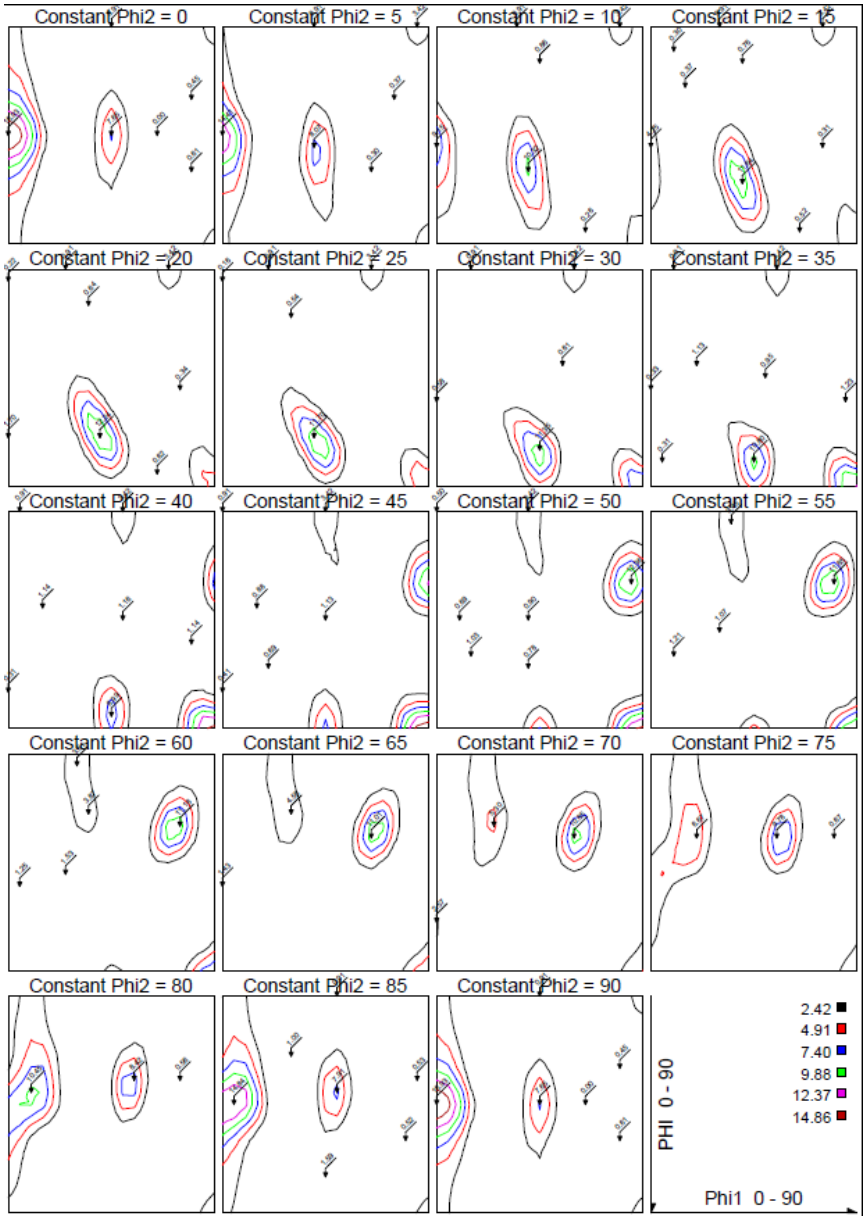

Figure 4.15: ODF obtained from XRD in the centre of a AA6082 plate rolled to 3mm

The deformation texture of the rolled sample rolled to a thickness of 3 mm is given in the form of an ODF in Figure 4.15. For this sample the true strain for rolling is given by Equation 2.2 and is equal to 0.98. One can here recognise that Goss is the most prominent orientation having a peak close to 16 times random. The Cube texture is weak having a peak below 4 times random. The ODF also shows a fibre, which is close to the β-fibre.

Here the peaks of the different texture components can be approximated as the following: Brass = 8, Copper = 14 and S= 10 rimes random.

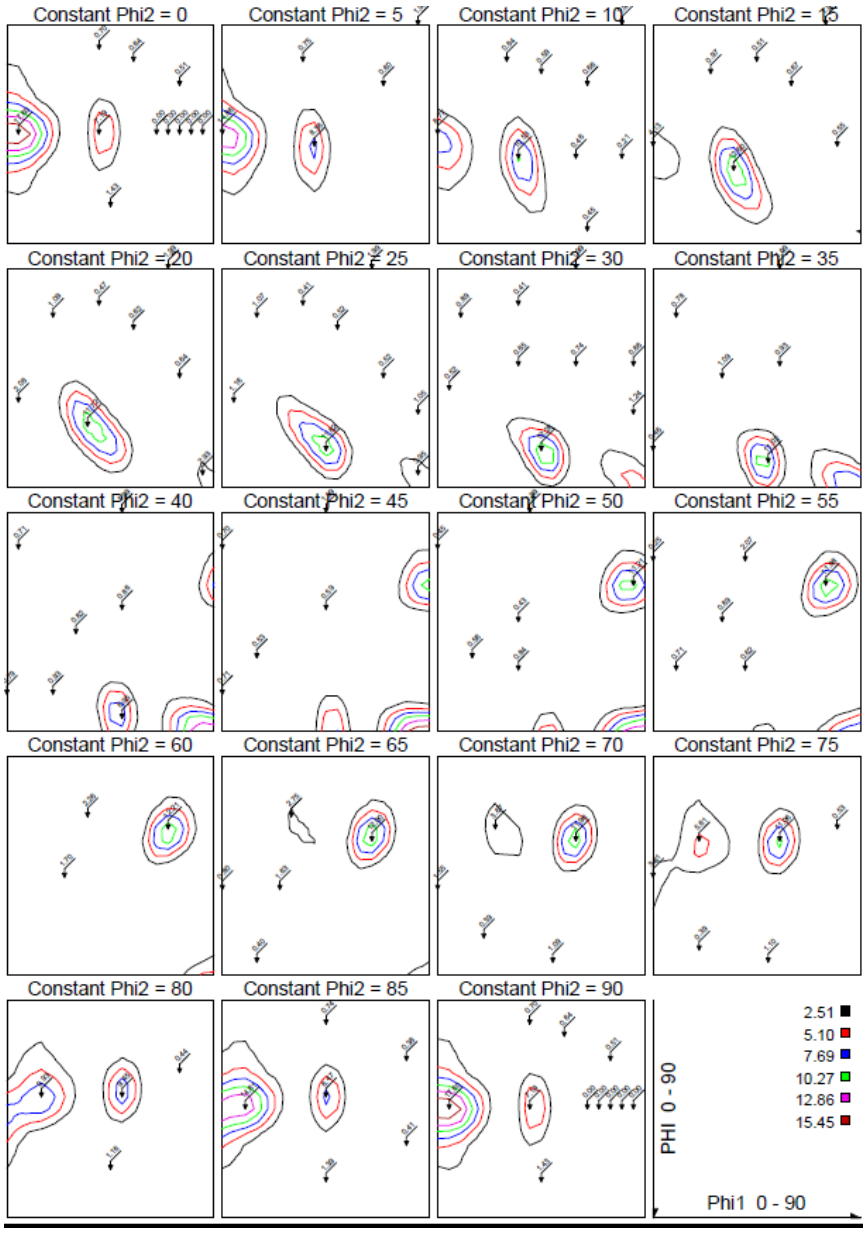

Figure 4.16: ODF obtained from XRD in the centre of a AA6082 plate rolled to 2mm

The deformation texture of the rolled sample rolled to a thickness of 2 mm is given in

the form of an ODF in Figure 4.16. For this sample the true strain for rolling is given by Equation 2.2 equal to 1.39. Goss is the most prominent texture component having a peak of 17.6 times random. The Cube component is non-existing in this material. The ODF also shows a fibre, which is closer to the β-fibre than in the less deformed plate. Here the peaks of the different texture components can be approximated as the following: Brass = 7, Copper = 11 and S= 12 times random.

AA6060 material

As for AA6082 8 mm thick section was cut out of the extruded AA6060 round profile and rolled to 2.7 mm and 2 mm. The rolling were carried out at room temperature. The data was collected from the centre of the rolled samples.

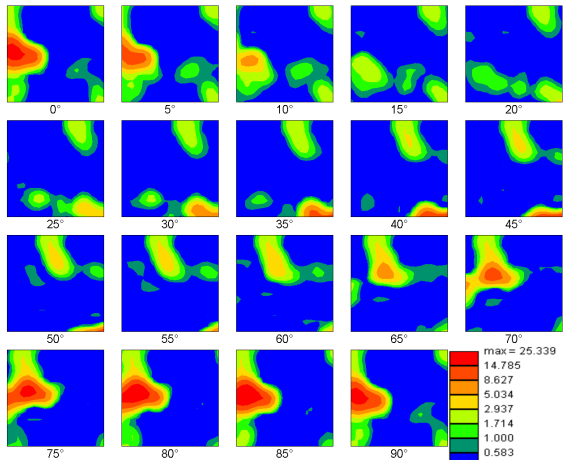

Figure 4.17: ODF obtained from EBSD in the centre of a AA6060 plate rolled to 2.7 mm

Figure 4.17 shows the ODF of the extruded AA6060 round profile material rolled to 2.7 mm. The main texture component for this sample is the Goss component which has a strength of 25 times random. There are also some weak Cube components.

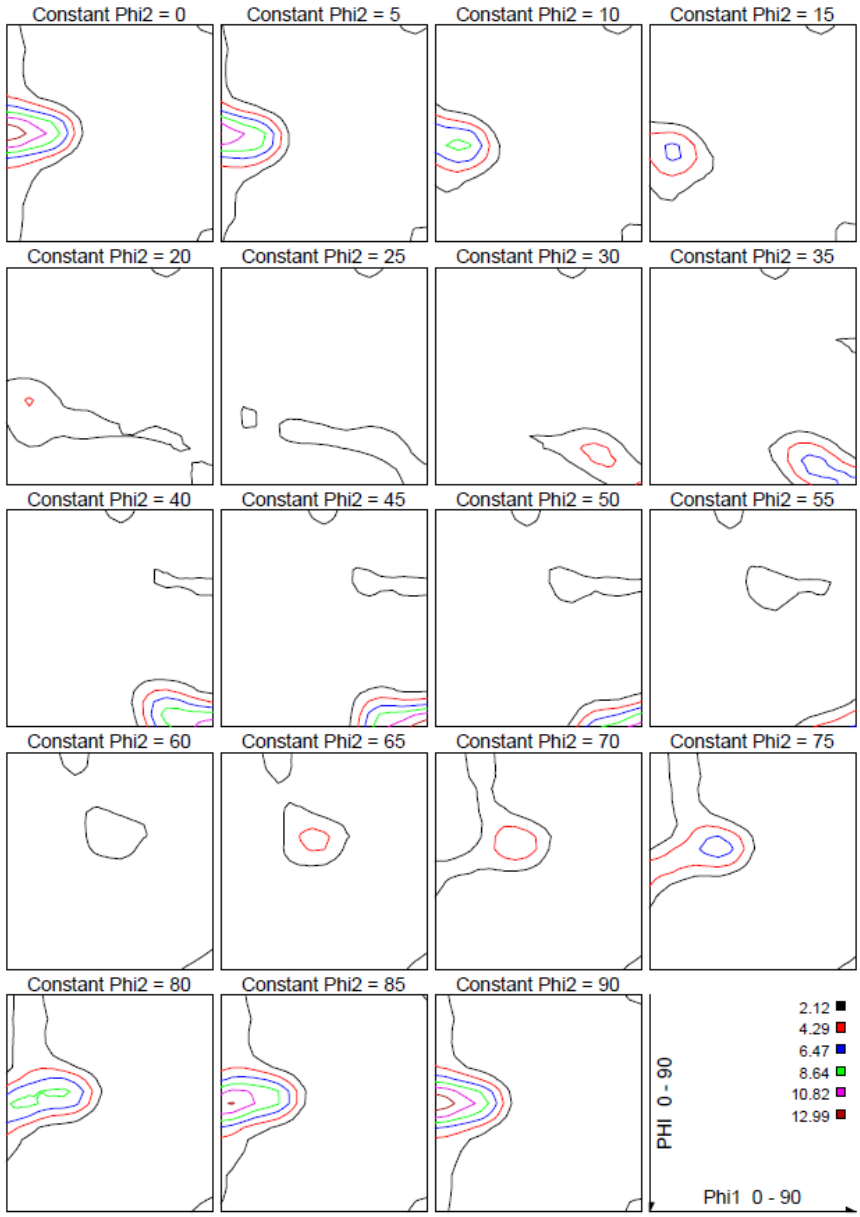

Figure 4.18: ODF obtained from EBSD, in the centre a AA6060 plate rolled to 2 mm

Figure 4.18 shows the ODF of the extruded AA6060 round profile material rolled to 2 mm. The main texture component of this sample is the Goss component. This component has an intensity of 13 times random. There are also some weak Cube components.

4.1.4 Annealed Samples

AA6082 material

The extruded AA6082 round profile material rolled to 3 mm and 2 mm, respectably, were annealed at 450°C and 550°C for 100 s.

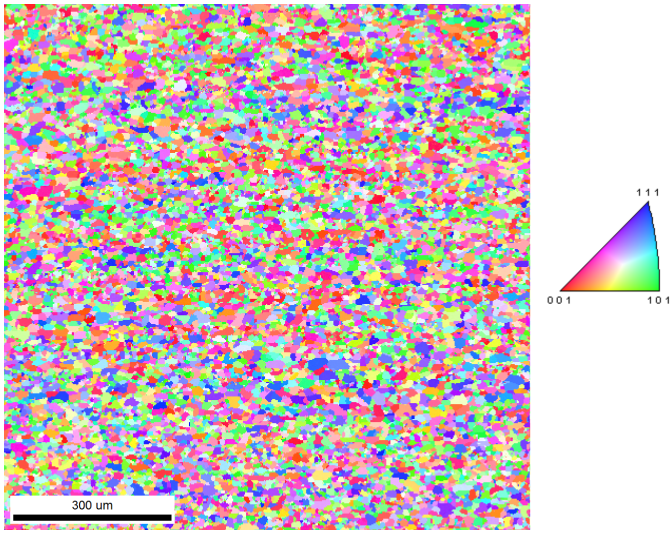

Figure 4.19: IPF micrograph of the centre of AA6082 extruded rod material rolled to 3 mm and annealed at 450°C for 100 s.

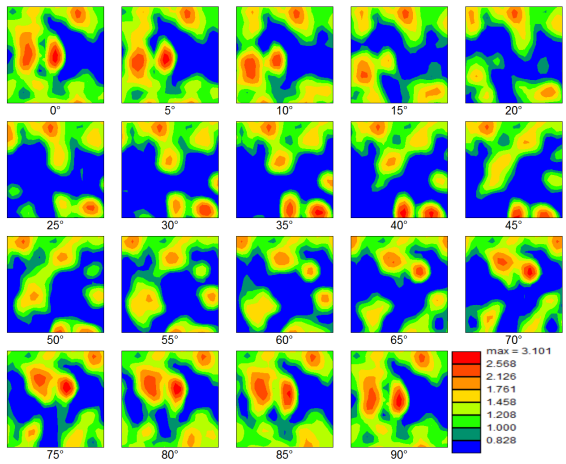

Figure 4.20: ODF obtained from the centre of AA6082 extruded rod material rolled to 3 mm and annealed at 450°C for 100 s.

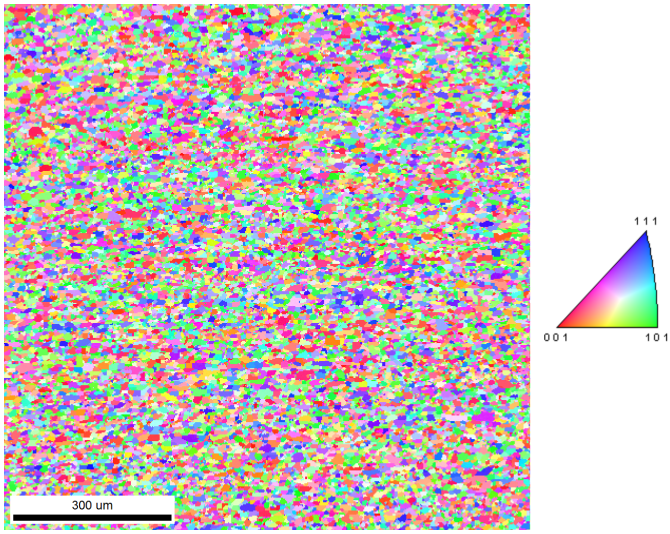

Figure 4.21: IPF micrograph from the centre of AA6082 extruded rod material rolled to 2 mm and annealed at 450°C for 100 s.

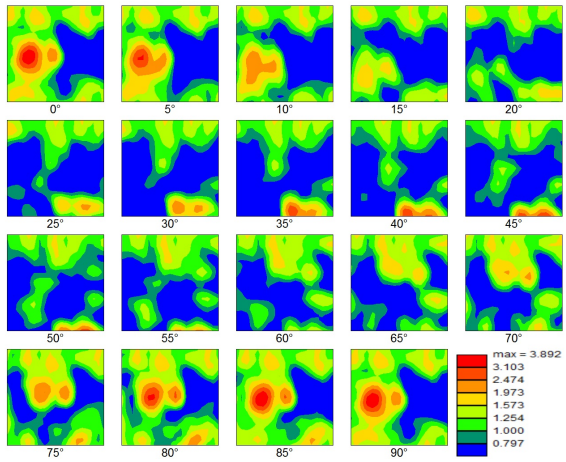

Figure 4.22: ODF obtained from the centre of AA6082 extruded rod material rolled to 2 mm and annealed at 450°C for 100 s.

Figure 4.20 and Figure 4.22 show the ODFs for the AA6082 samples rolled to 3 mm and 2 mm and annealed at 450°C. The texture is weak for both samples and show some ND-rotated Cube composition. The most prominent peaks are two fibres which start close to the centre in the section where $\phi_2 = 0°$. One of these fibres is the β-fibre. The β-fibre has strongest intensity at the Brass component, the intensity is lower at the S component and there are almost no Copper component. The recrystallised grains are very small in these samples as seen in Figure 4.21 and Figure 4.21. The grain size is 8.0 ± 4.1 μm for

the sample rolled to 3 mm and 6.7 ± 3.1 μm for the sample rolled to 2 mm.

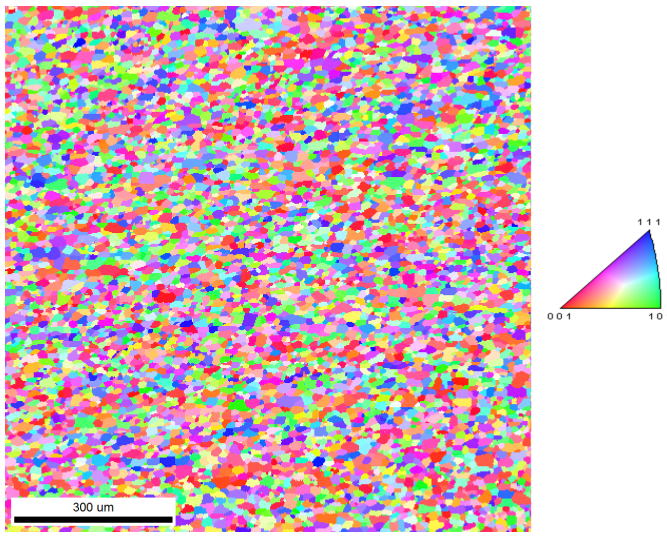

Figure 4.23: IPF micrograph obtained from the centre of AA6082 extruded rod material rolled to 3 mm and annealed at 550°C for 100 s.

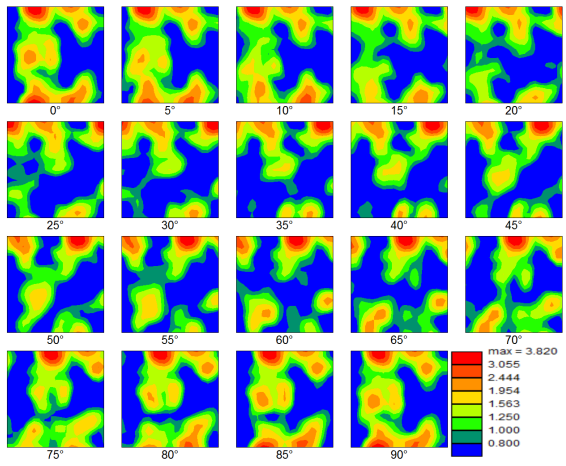

Figure 4.24: ODF obtained from the centre of AA6082 extruded rod material rolled to 3 mm and annealed at 550°C for 100 s.

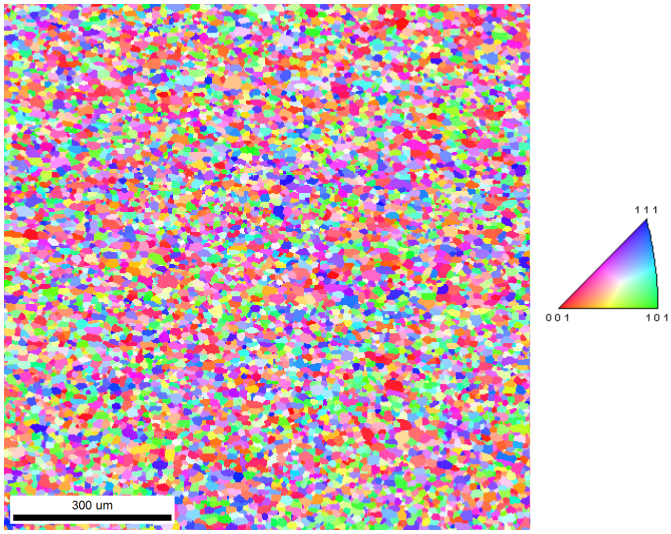

Figure 4.25: IPF micrograph from the centre of AA6082 extruded rod material rolled to 2 mm and annealed at 550°C for 100 s.

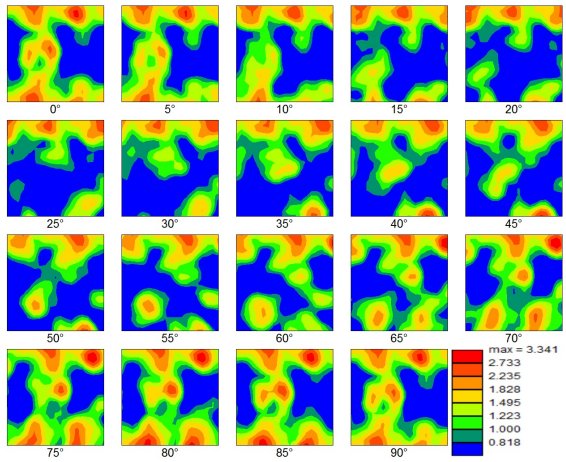

Figure 4.26: ODF obtained from the centre of AA6082 extruded rod material rolled to 2 mm and annealed at 550°C for 100 s.

Figure 4.24 and Figure 4.24 show the ODFs for the AA6082 samples rolled to 3 mm and 2 mm and annealed at 550°C. The textures of these samples are similar to the textures of the samples annealed at 450°C in that they are weak and has ND-rotated cube components. They differs from the ODFs 4.22 and 4.20 in that they have weaker fibres, including the β-fibre, near the centre of the section with $\phi_2 = 0°$. The recrystallised grains are small as seen in Figure 4.23 and Figure 4.23. The grain size is 10.4 ± 4.9 μm for the sample rolled to 3mm and 9.9 ± 4.4 μm for the sample rolled to 2 mm.

AA6060 material

The extruded AA6060 round profile material rolled to both 2.7 mm and 2 mm were annealed at 450°C and 550°C for 100 s. The sample rolled to 2 mm and annealed at 450°C for 100 s are annealed for 10 more minutes at 450°C.

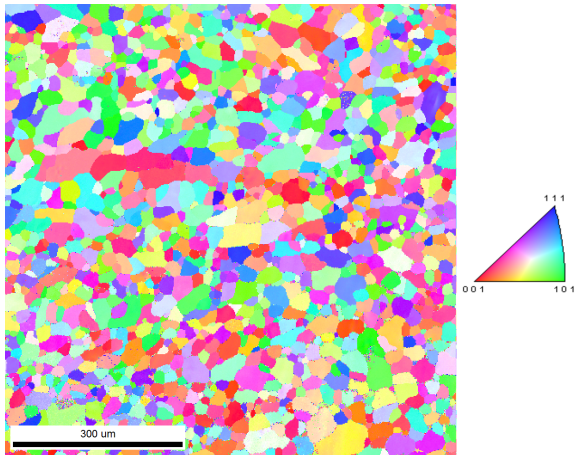

Figure 4.27: IPF micrograph obtained from the centre of AA6060 extruded rod material rolled to 2.7 mm and annealed at 450°C for 100 s.

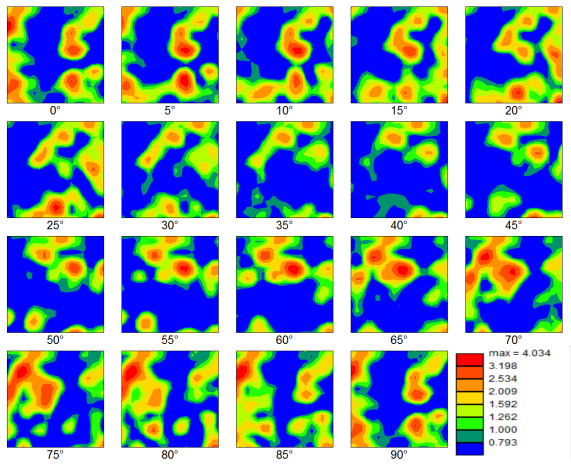

Figure 4.28: ODF obtained from the centre of AA6060 extruded rod material rolled to 2.7 mm and annealed at 450°C for 100 s.

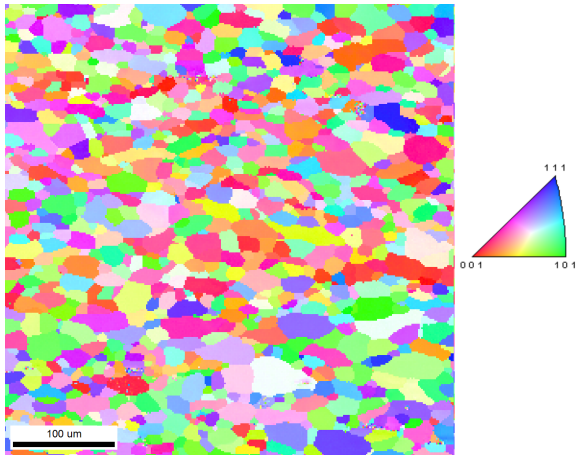

Figure 4.29: IPF micrograph obtained ffrom the centre of AA6060 extruded rod material rolled to 2 mm and annealed at 450°C for 100 s.

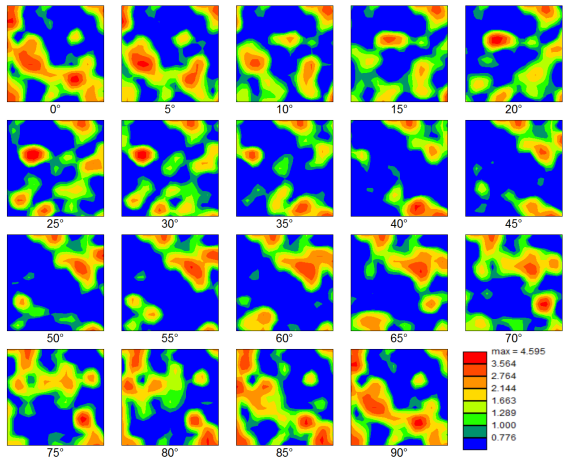

Figure 4.30: ODF obtained from the centre of AA6060 extruded rod material rolled to 2 mm and annealed at 450°C for 100 s.

Figure 4.28 and Figure 4.30 show the texture of the AA6060 plates rolled to 2 mm and 2.7 mm respectively after annealing at 450°C for 100 s. Both ODFs show a weak texture having max intensity of about 4 times random. There are also peaks for an ED rotated Cube component in both ODFs. The IPF micrographs of these figures are given in Figure 4.29 and Figure 4.27. These figures shows recrystallised microstructures The grain size is 16.4 ± 11.2 μm for the sample rolled to 2.7 mm and 12.5 ± 6.9 μm for the sample rolled to 2 mm.

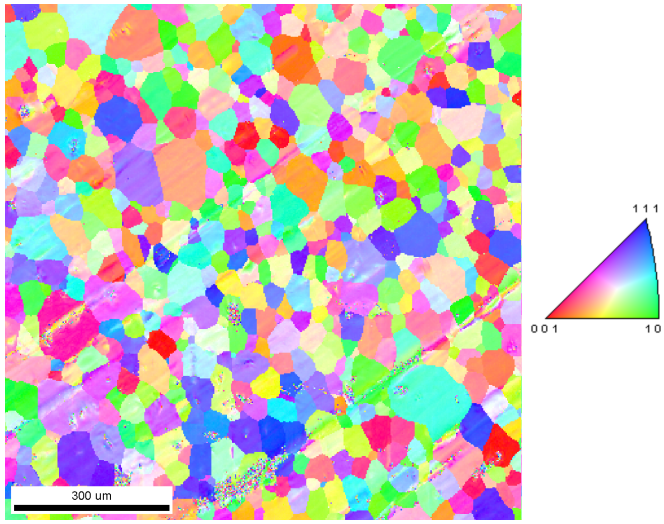

Figure 4.31: IPF micrograph from the centre of AA6060 extruded rod material rolled to 2.7 mm and annealed at 550°C for 100 s.

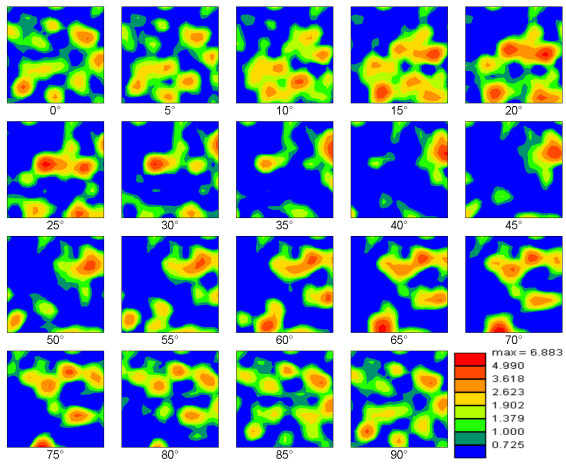

Figure 4.32: ODF obtained from the centre of AA6060 extruded rod material rolled to 2.7 mm and annealed at 550°C for 100 s.

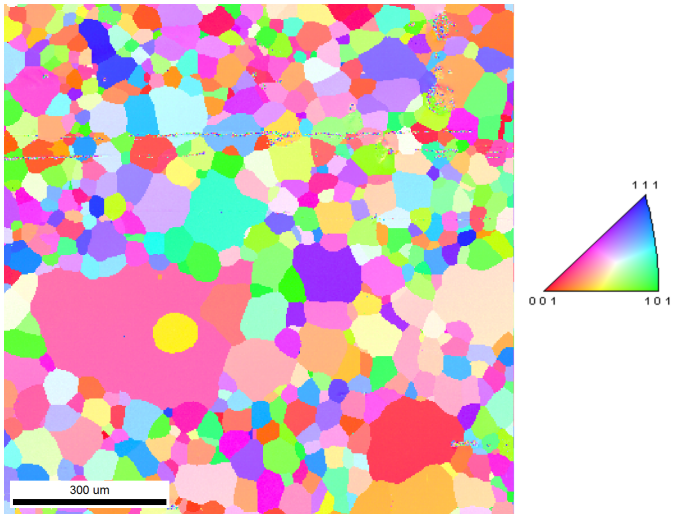

Figure 4.33: IPF micrograph from the centre of AA6060 extruded rod material rolled to 2 mm and annealed at 550°C for 100 s.

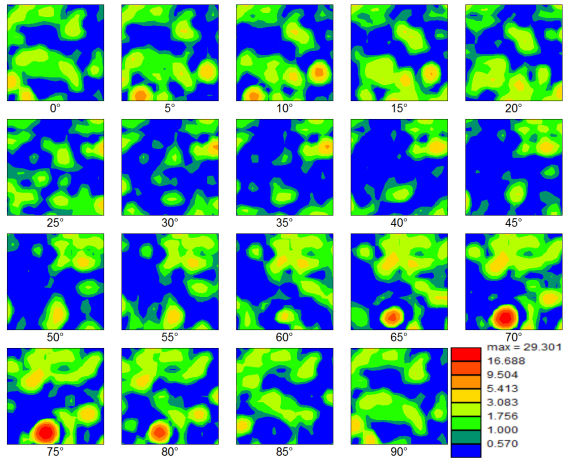

Figure 4.34: ODF obtained from the centre of AA6060 extruded rod material rolled to 2 mm and annealed at 550°C for 100 s.

Figure 4.32 and figure 4.34 show the ODFs to the AA6060 samples rolled to 2.7 mm and 2 mm respectively and annealed at 550°C for 100 s. Figure 4.31 and Figure 4.33 show the inverse pole figure of the samples shown by ODF in Figure 4.32 and Figure 4.34. The microstructures observed are clearly recrystallised microstructures. Figure 4.32 shows a weak texture with max intensity of a bit under 7 times random. The grains are quit large as we recognice in Figure 4.32. The sample rolled to 2 mm shows a stronger texture. This may be because of the large grains shown in Figure 4.33. These big grains may be a sign

of abnormal grain growth. The grain size is 26.5 ± 21.7 μm for the sample rolled to 2.7 mm and 33.3 ± 25.1 μm for the sample rolled to 2 mm.

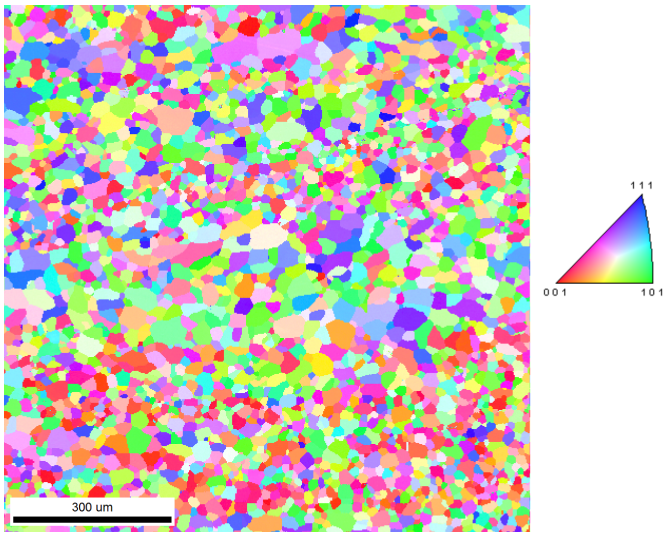

Figure 4.35: IPF micrograph from the centre of AA6060 extruded rod material rolled to 2 mm and annealed at 450°C for 100 s and further annealed at 450°C for 10 minutes.

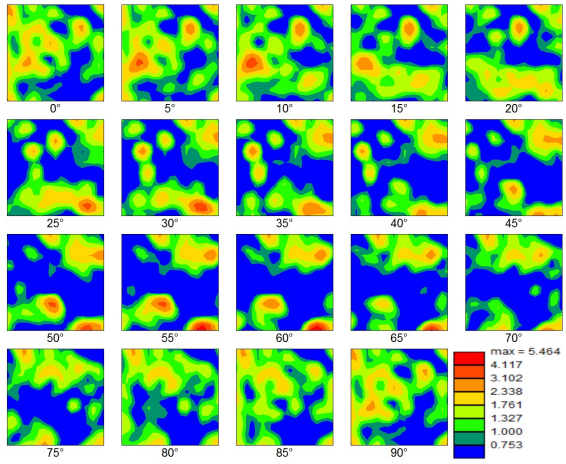

Figure 4.36: ODF obtained from the centre of AA6060 extruded rod material rolled to 2 mm and annealed at 450°C for 100 s and further annealed at 450°C for 10 minutes.

Figure 4.35 shows the IPF-micrograph for the centre of the AA6060 extruded cylindrical rod material rolled to 2 mm and annealed at 450°C for 100 s before further annealed at 450°C for 10 minutes. The microstructure are clearly recrystallised. The ODF (Figure

4.36) shows a weak texture with peak intensity of 5.5 times random. Some Cube components with an intensity of almost 2 can be recognised. The grain size is 16.7 ± 9.3 μm. Some larger grain can be observed towards the centre of Figure 4.35 which may be a sign of further grain growth during the second annealing phase.

4.2 Simulation of deformation textures

Crystal plasticity modeling of texture evolution were done using VPSC and ALAMEL. During the VPSC modeling interaction scheme (Equation 2.19 and Equation 2.20), the strain rate sensitivity (m) (n is contained in the interaction scheme equation and the relationship between n and m is $n = 1/m$) and the active slip systems (Given as slip system group Table 3.3) were varied. In the ALAMEL simulations active slip systems and relaxations were varied. All simulations used deformation velocity gradients based on FEM simulations discussed in Chapter 4.2.1.

4.2.1 Analysis of deformation modes during flat profile extrusion

With the COSMETEX project, a mini-flat profile of thickness 1.3 mm and width 5.5 mm was extruded at SAPA Technology from billet diameter 200 mm. The material was AA6063. The average accumulated strain was about 4 in the center of profile. The extrusion die has a pocket of 1 mm , and a 3 mm long parallel bearing. Because of its relevance for COSMETEX has this extrusion process been simulated. The simulation was performed by Dr. T. Aukrust from Sintef Materials and Chemistry, Oslo. The results of this simulation are used as motivation for texture simulations done in this work. The FEM mode and a region of the FEM mesh are shown in Figure 4.37. Due to the symmetry, only one quarter of the billet and profile were considered. Deformation histories along 9 different prticle paths have been exported from the flow simulation, for the purpose of analysis of deformation modes during extrusion. The trajectory of the nine particle paths are illustrated in Figure 4.38. the pocket is positioned between -3 and -4 mm.

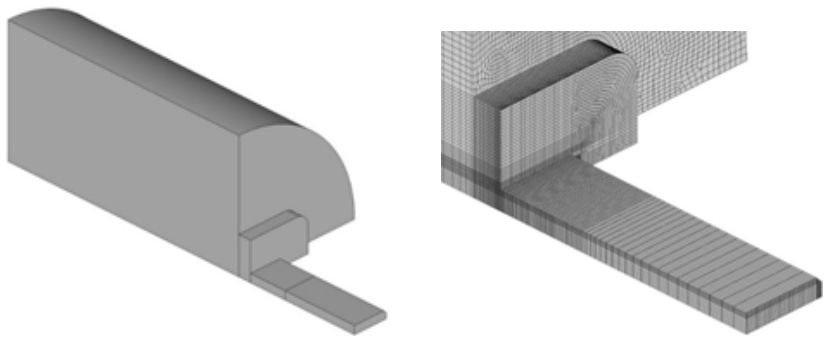

(a) **(b)**

Figure 4.37: The FEM model **(a)** and FEM mesh **(a)** employed for the flow simulation of mini flat profile extrusion.

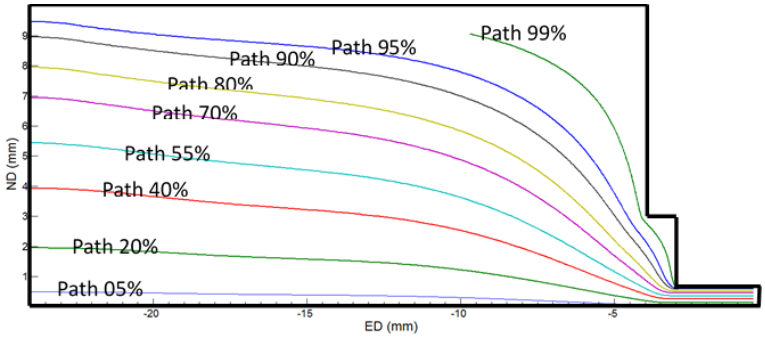

Figure 4.38: Trajectory of particle paths along which deformed history has been exported in FEM flow simulation.

The analysis of deformed mode during extrusion, used as motivation for the texture simulations, was focused on the centre region of the profile (Path 0.05 in Figure 4.38). The evolution of strain rate component during extrusion along Path 0.05 is plotted in Figure 4.39. The strain rate components related with shear deformatio which are D_{12}, D_{23} and D_{13} are much smaller than D_{11} and D_{33}. This indicates that the shear deformation is insignificant for the center regions of the profile. It is also noted that D_{11} and D_{33} are close in magnitude but of opposite signs and the ration $D_{22}/D_{33} \approx 0$ near the pocket region. This is the deformation mode of plane strain deformation, which is the deformation mode of rolling. Figure 4.40 shows that the ratio D_{22}/D_{33} evolves during extrusion. Here are $\alpha = D_{22}/D_{33}$. It is shown there that at strains less than 2 the ration D_{22}/D_{33} are so close that the material can be said to experience uni-axial tensile deformation.

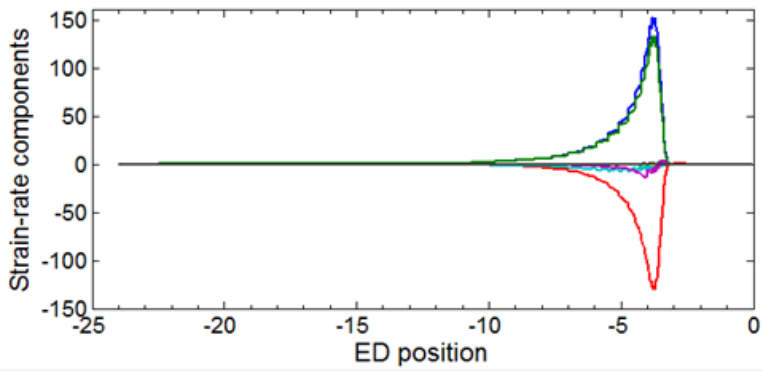

Figure 4.39: Evolution of strain-rate component along particle path 0.05.

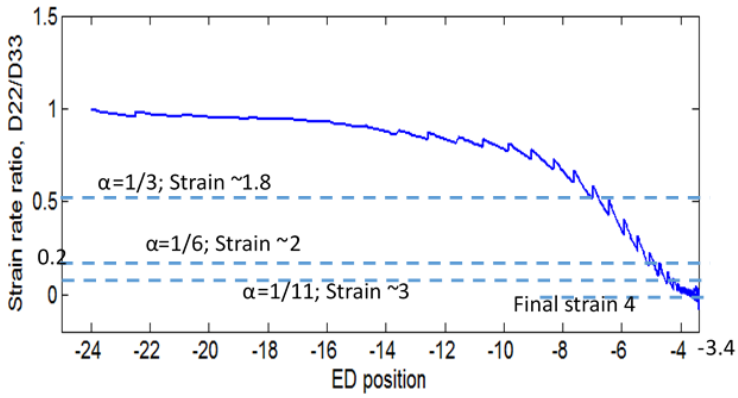

Figure 4.40: Evolution of strain-rate component along particle path 0.05.

As seen above, the material which ended in the centre of the current flat profile would have experienced uni-axial tensile deformation in the container and close to plane strain deformation near or in the pocket. in other words, the deformation mode during extrusion for the current flat profile is firstly uni-axial tensile deformation and followed by plane strain deformation.

4.2.2 Overview of performed texture simulation

The different simulations using VPSC done are represented as a flowchart in Figure 4.41. The input textures are random texture (input in uni-axial tensile deformation) and fibre texture (input in plane strain deformation and modified plane strain deformation). Random texture is a texture where the grains initially are randomly orientated. This is an approximation of the texture obtained after casting of extrusion billets. The Fibre texture is divided into a $\langle 100 \rangle$-fibre and a $\langle 111 \rangle$-fibre texture component. The ODFs of these fibres are illustrated in Figure 4.42. Both fibres has a density evenly distributed along the whole fibre.The $\langle 111 \rangle$-fibre contains both Cube and Brass components. The $\langle 111 \rangle$-fibre is similar to the β-fibre, but has a higher ϕ_1 value for the Brass and S components.

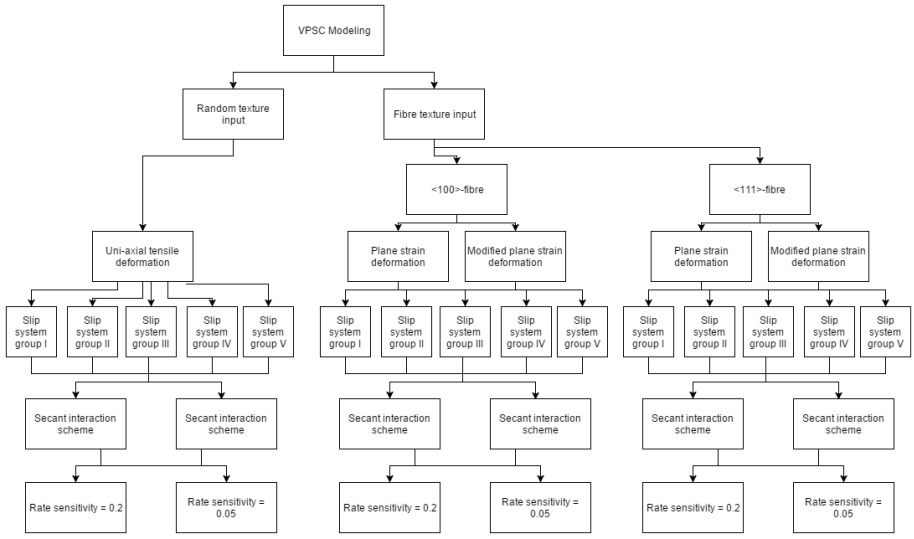

Figure 4.41: Flowchart describing the different simulation done by VPSC.

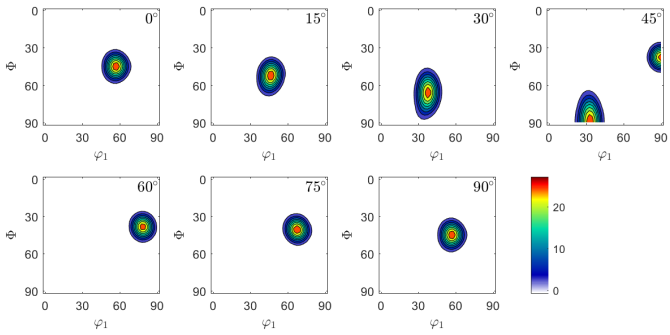

(a)

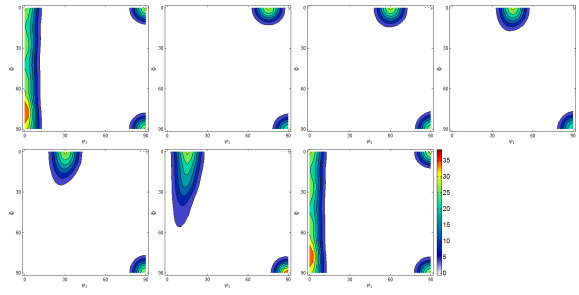

(b)

Figure 4.42: ODFs of the **(a)**⟨100⟩-fibre and the **(b)**⟨111⟩-fibre used as input orientation in the plane strain simulation

The random texture simulations use velocity gradients as in Figure 4.1 where D_{22} = D_{33} = -0.5 (uni-axial deformation). This deformation gives fibre textures because of the axi-symmetrical deformation. The fibre texture simulations are carried out using velocity gradients in Table 4.1 where D_{22} = 0 and D_{33} = -1 for plane strain deformation and D_{22} = -0.2 and D_{33} = -0.8 for modified plane strain deformation. For the plane strain deformation simulations were also done covering different total true strain ranging from 0.8 to 2. The uni-axial tensile deformation and modified plane strain deformation where only done with a total true strain of 2. All simulations where carried out using all different slip system groups given in Table 3.3, both interaction schemes (Tangent and secant) and two different strain rate sensitivities (0.2 and 0.05).

Table 4.1: Velocity gradients showing D22 and D33.

Velocity gradient		
1	0	0
0	D_{22}	0
0	0	D_{33}

4.2.3 Uni-axial Tensile Deformation

VPSC Simulations

VPSC simulations were done using a random texture as input texture and uni-axial tensile deformation (Table 2.4). Slip system group (Table 3.3), interaction scheme and rate sensitivity (Equation 2.19 and Equation 2.20) were varied. The different simulation were evaluated by fraction of $\langle 100 \rangle$-fibre texture and $\langle 111 \rangle$-fibre texture.

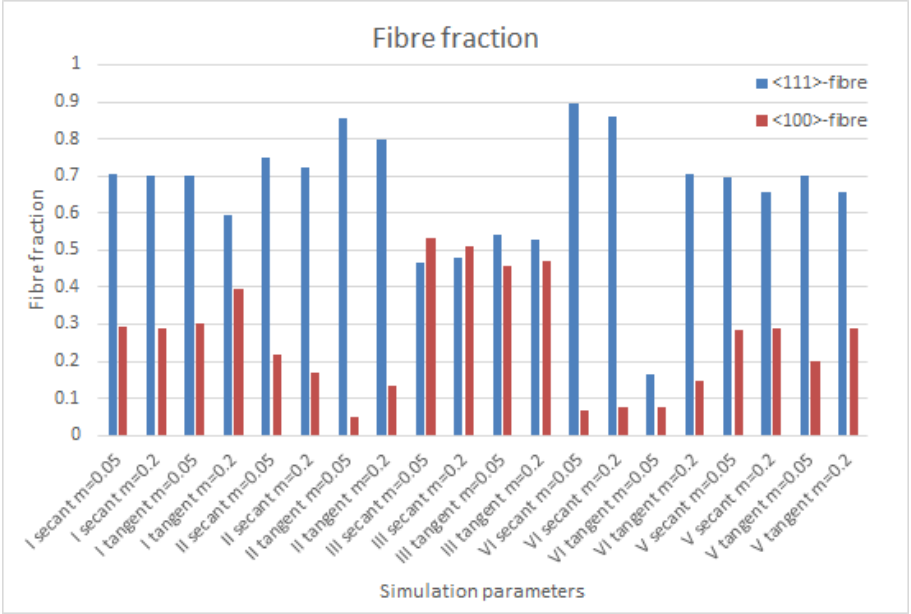

Figure 4.43: Simulated fibre fraction after uni-axial tensile deformation.

The simulated fibre fraction is given in Figure 4.43. The slip-system group notes the activated slip-system according to table 3.3. The figure shows that in most cases $\langle 111 \rangle$-fibre is the dominating fibre texture (fraction > 0.5), while the $\langle 100 \rangle$-fibre texture fraction varies in the range 0 0.5.

Slip system group III, were the $\{112\}\langle 110 \rangle$ and the $\{111\}\langle 110 \rangle$ slip systems are active, has the most $\langle 100 \rangle$-fibres. Here there are about 0.5 of both type of fibres. Simulations at other sets of activated slip system had around a fraction of 0.7 of $\langle 111 \rangle$-fibres. The $\langle 100 \rangle$-fibre has a fraction of 0.1 to 0.3 in these cases.

ALAMEL simulations

ALAMEL simulations were done using a random texture as input texture and deformation gradients give in Table 2.4. Slip system group (Table 3.3) were varied and different relaxations were used. These simulations were evaluated by fractions of $\langle 100 \rangle$-fibre texture and $\langle 111 \rangle$-fibre texture.

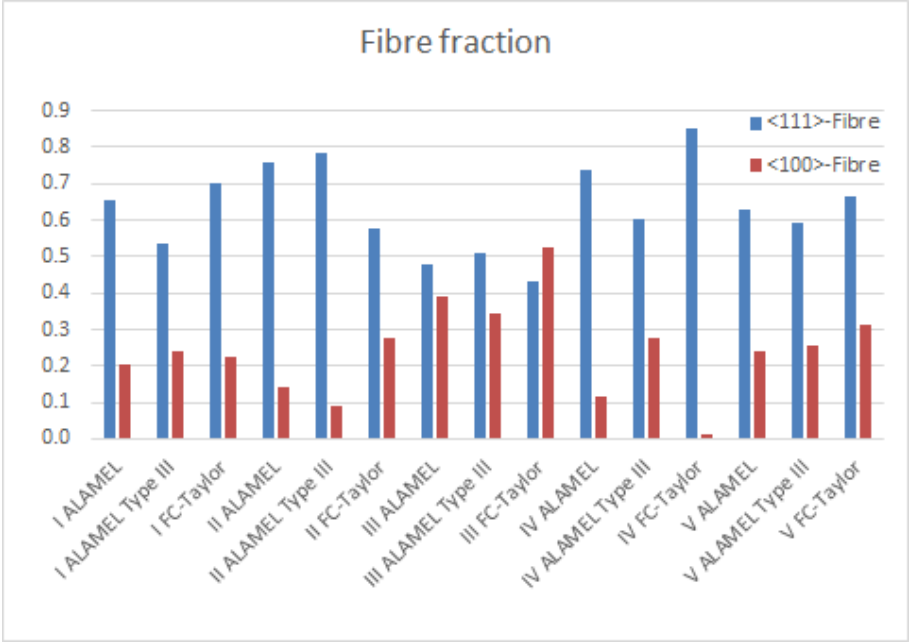

Figure 4.44: Simulated fibre fraction after uni-axial tensile deformation using the ALAMEL software.

The fraction of the different fibres in the simulation done by using ALAMEL is shown in Figure 4.44. Slip system group III has the highest fraction of $\langle 100 \rangle$-fibres and lowest amount of $\langle 111 \rangle$-fibres. FC-Taylor has the largest fraction $\langle 100 \rangle$-fibres using slip system group III with 0.525. Both ALAMEL and ALAMEL Type III have a fraction between 0.3 and 0.4 of $\langle 100 \rangle$-fibres. In ALAMEL Type III we see a increase of 0.1 in fraction $\langle 100 \rangle$-fibres when including the $\{112\}\langle 110 \rangle$ slip system and in ALAMEL we see an increase of 0.19, compared with FC-Taylor were we see a increase of 0.3.

4.2.4 Plane Strain Deformation

VPSC Simulations

VPSC simulations were done using $\langle 111 \rangle$-fibre texture and $\langle 100 \rangle$-fibre texture as input and plane strain deformation gradients (Table 2.5). Slip system group (Table 3.3), interaction scheme and rate sensitivity (Equation 2.19 and Equation 2.20) were varied. The deformed $\langle 111 \rangle$-fibre texture simulations are evaluated by comparing the resulting fibre to the β-fibre obtained experimentally. The deformed are evaluated by the strength of Goss and Cube components. The simulations obtained using slip system group I are examined closer to easier compare to the rolled textures.

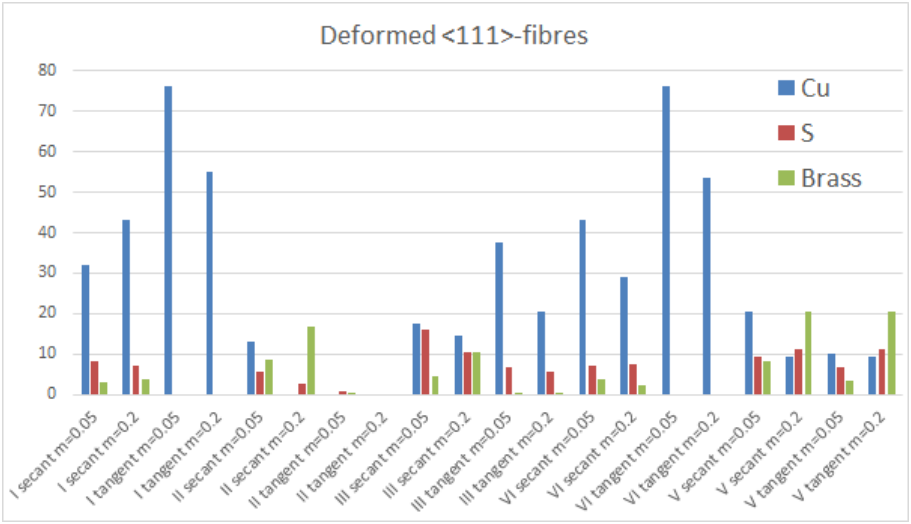

Figure 4.45: Simulated component intensity of deformed $\langle 111 \rangle$-fibre.

Figure 4.45 shows the density of different orientations in an ODF for simulations of the rolling of the $\langle 111 \rangle$-fibre. The true strain is equal to 2 in these simulations. Most simulations show a dominance of Cu fibres. The lack of the other orientations of the β-fibre is because the fibre in these textures is closer to the $\langle 111 \rangle$-fibre. This means that the values obtained from the ODFs in this figure do not give a good picture of the intensities along the existing fibre. Slip system II with tangent interaction has a texture which are close to random. Secant scheme for slip system group III has close to equal intensity of Copper and S components. The simulation done with a strain rate sensitivity of 0.2 has also a high density of Brass oriented grains. The simulation done using slip system group V has Brass as the dominating texture component having an intensity twice the intensity of both Copper and S. The last two components are about equal in intensity.

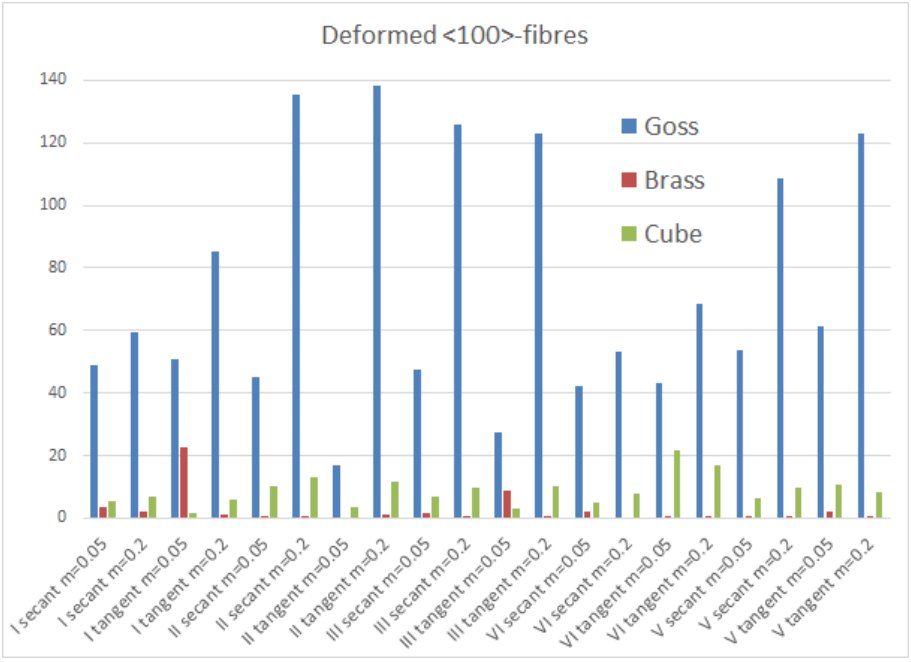

Figure 4.46: Simulated component intensity of deformed ⟨100⟩-fibre.

Figure 4.46 shows different peaks in an ODF for the rolling simulation of the ⟨100⟩-fibre. The true strain is equal to 2 for these simulations. Goss is the dominating texture component for all simulations and Cube is the second strongest component for almost all of the simulations done with plane strain. Highest amount of Cube can be seen for the simulation done with slip system group IV and tangent interaction scheme.

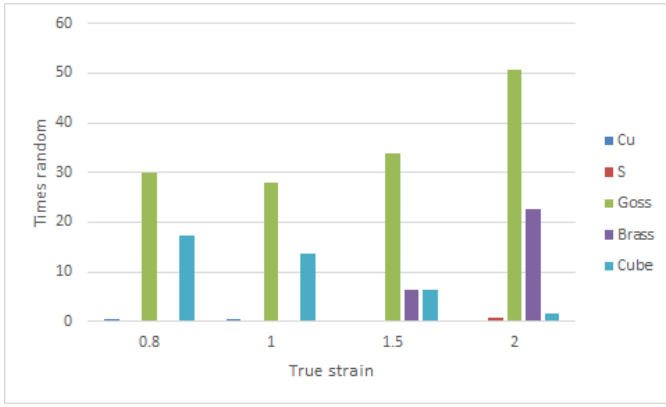

Figure 4.47: Intensity peaks of different components for different simulation using different true strain.

Figure 4.47 shows how the texture for $\langle 100 \rangle$-fibre evolve by rolling with increasing true strain. From this figure one can see that an increase truea strain decreases the amount of Cube. The amount of Goss oriented grains on the other hand increases with increases total deformation.

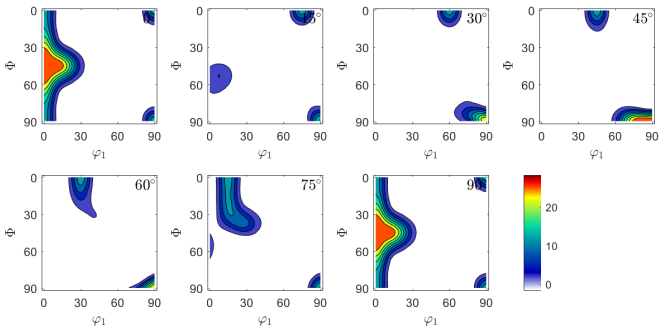

(a)

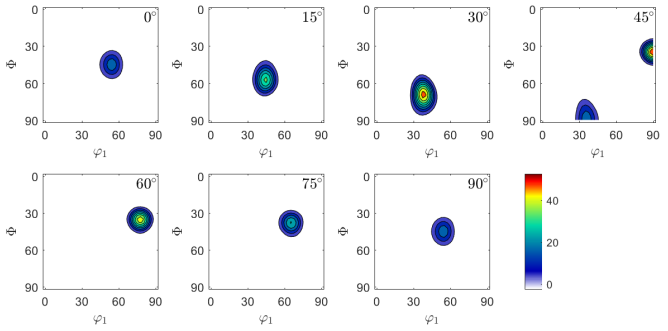

(b)

Figure 4.48: Simulated ODF for **(a)**$\langle 100 \rangle$-fibre and **(b)**$\langle 111 \rangle$-fibre deformed having a true strain of 1. The simulation is of type I using tangent interaction scheme and a strain rate sensitivity of $m = 0.05$

Figure 4.48 shows the simulated ODF for plane strain deformation $\langle 100 \rangle$-fibre and $\langle 111 \rangle$-fibre using the tangent interaction scheme and rate sensitivity of $m = 0.05$. Here the true strain is equal to 1. This elongation is close to the calculated elongation for the plate rolled to 3 mm which has an ODF as shown in Figure 4.15.

The deformed $\langle 100 \rangle$-fibre has Goss as the most prominent orientation having a peak intensity close to 28 times random. There are also some Cube orientated grains with peak intensity close to 14 times random. Both the Cube and the Goss is part of the $\langle 100 \rangle$-fibre, which is clearly shown in this ODF.

The deformed $\langle 111 \rangle$-fibre shows a texture where the orientations are close to the input $\langle 111 \rangle$-fibre. It contains different orientations than that of the β-fibre commonly seen in a rolled texture and which also can be found in the rolled texture obtained from XRD shown in Figure 4.15. Some comparisons between simulated and experimental data can be done

by comparing the intensity along the fibres. For easier comparison with the experimental results, different intensities along the fibre obtained by simulations are compared with "equalent" components in the β-fibre. If we say that Brass equivalent is the β-fibre component located near the centre at $\phi_2 = 90°$ and S equivalent is located close to $\phi_2 = 60°$ and Copper equivalent is located to the right at $\phi_2 = 45°$, then values for the different components of β-fibre are approximately: Brass= 20, S=35 and Cu=55. This result shows significant increase in the Copper equivalent, slight increase in the S equivalent and a decrease in the Brass equivalent as compared to the input texture.

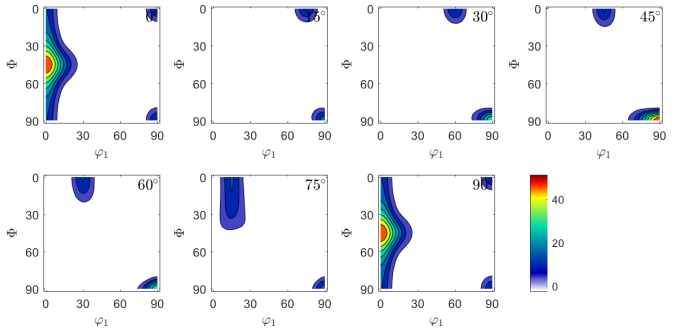

(a)

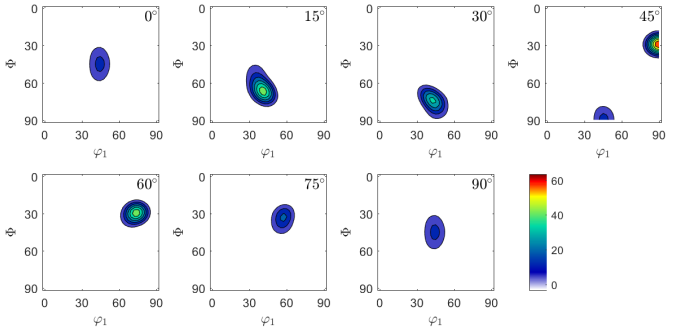

(b)

Figure 4.49: Simulated ODF for **(a)**$\langle 100 \rangle$-fibre and **(b)**$\langle 111 \rangle$-fibre deformed using a true strain of 1. The simulation is of type I using the secant interaction scheme and a strain rate sensitivity of $m = 0.05$

Figure 4.49 shows the simulated ODF for plane strain deformation $\langle 100 \rangle$-fibre and $\langle 111 \rangle$-fibre with the tangent interaction scheme and strain rate sensitivity of $m = 0.05$. All other simulation parameters, except for the interaction scheme, are equal to the parameters used to make Figure 4.48.

The ODF obtained from deforming the $\langle 100 \rangle$-fibre shows the Goss and Cube texture. The Goss texture peaks are at about 50 times random and the Cube texture peaks are at 16 times random. Both texture components are stronger than they are in the texture obtained by using the tangent interaction scheme, but there is also a larger difference between the

intensity of the Goss and the Cube. The $\langle 100 \rangle$-fibre is more concentrated at the Goss orientation.

The deformed $\langle 111 \rangle$-fibre obtained by using the secant interaction scheme is displaced a bit towards the left compared to the ODF obtained by using the tangent scheme. However, it is not sufficiently displaced to be located in the same position as the β-fibre components. The equivalent texture components are as follow: Copper = 60 times random, Brass = 10 times random and S = 30 times random. This means that the deformation has increased the intensity of the copper equivalent and decreased the intensity of the Brass equivalent.

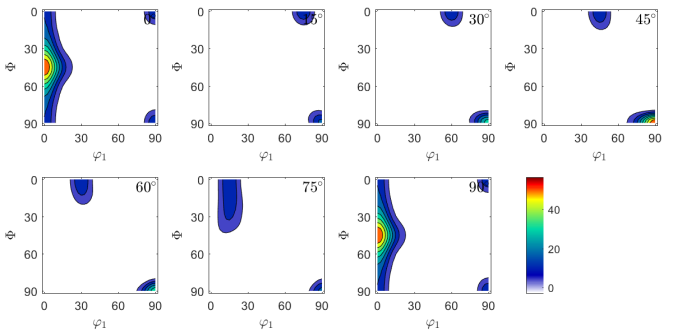

(a)

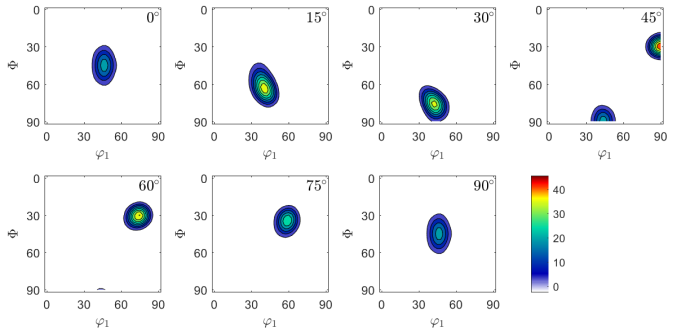

(b)

Figure 4.50: Simulated ODF for **(a)**$\langle 100 \rangle$-fibre and **(b)**$\langle 111 \rangle$-fibre deformed using a true strain of 1. The simulation is of type I using secant interaction scheme and a strain rate sensitivity of $m = 0.2$.

Figure 4.50 shows the simulated deformation with simulation parameters equal to those used to get Figure 4.48 except that the strain rate sensitivity is 0.2 instead of 0.05. The deformed $\langle 100 \rangle$-fibre simulated with $n = 0.2$ is almost similar to the one simulated with $n = 0.05$ with Cube = 56 times random and Goss = 17 times random. The simulated deformed $\langle 100 \rangle$-fibre with $n = 0.2$ is in the same location as the deformation texture components simulated with $n = 0.05$, but the intensities along the fibre are different with Brass = 25, S = 35 and Copper =45.

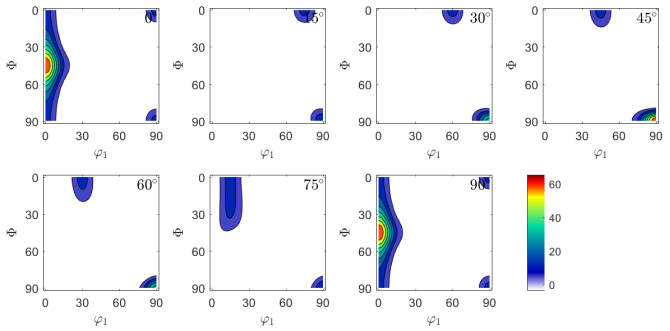

(a)

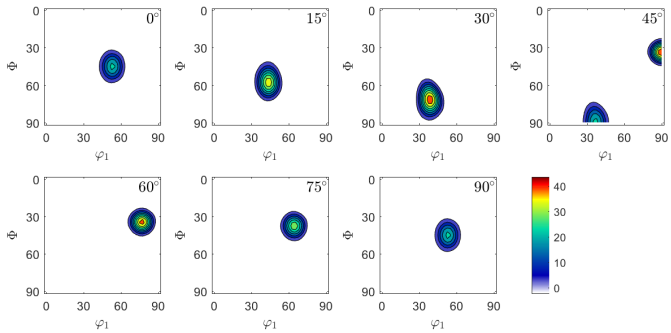

(b)

Figure 4.51: Simulated ODF for **(a)**$\langle 100 \rangle$-fibre and **(b)**$\langle 111 \rangle$-fibre deformed with a true strain of 1. The simulation is of type I using tangent interaction scheme and a strain rate sensitivity of $m = 0.2$.

Figure 4.51 shows the simulations using $m = 0.2$ with the tangent interaction scheme. Here the $\langle 111 \rangle$-fibre is also at the same locations as when $m = 0.05$ and the peak intensities along the fibre is different from the experimental β-fibre. The peaks for Copper and S is about 40 times random and Brass is 25 times random. The ODF of the deformed $\langle 100 \rangle$-fibre looks more like the ones obtained by using the secant interaction schema than the ODF obtained by using the tangent interaction scheme and $m = 0.05$. Here Cube is 65 times random and Goss 16 times random.

Modified plane strain deformation

Simulations using deformed $\langle 100 \rangle$-fibre texture, and secant interaction scheme are shown using both a rate sensitivity of 0.05 and 0.02. First simulations using a modified plane strain deformation gradients (Table 3.2) are presented before the same simulations using plane strain deformation gradients (Table 3.2) are presented. These simulation are evalued by amount Cube and Goss Texture components.

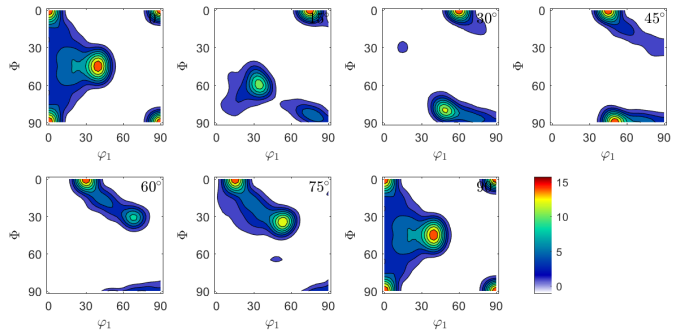

(a)

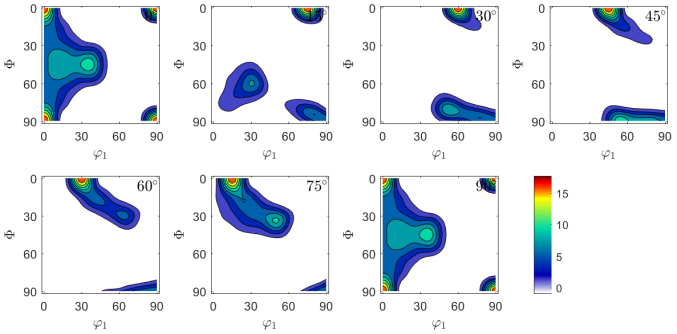

(b)

Figure 4.52: Simulated ODF for $\langle 100 \rangle$-fibre deformed using a true strain of 2. The simulation is of type IV using secant interaction scheme and a strain rate sensitivity of $m = 0.05$**(a)** and $m = 0.2$**(b)**. The deformation gradient for these simulations are given in Table 3.2.

Figure 4.52 shows the ODFs for simulations done with velocity gradients given in Table 3.2. These simulation were done with the secant interaction scheme and the strain rate sensitivity was $m = 0.05$ **(a)** and $m = 0.2$ **(b)**. In these simulations are the Cube component and the Brass component the strongest texture components. The Cube component is the strongest component in the simulation done with a rate sensitivity of 0.2 where it is 18 times random. Here the Brass component is equal to 10 times random. For the simulation done with a rate sensitivity of 0.05 has the intensity of the Cube component is equal to 16 times random and the intensity of Brass component equal 13 times random. We can also see that the Brass component continue into a β-fibre.

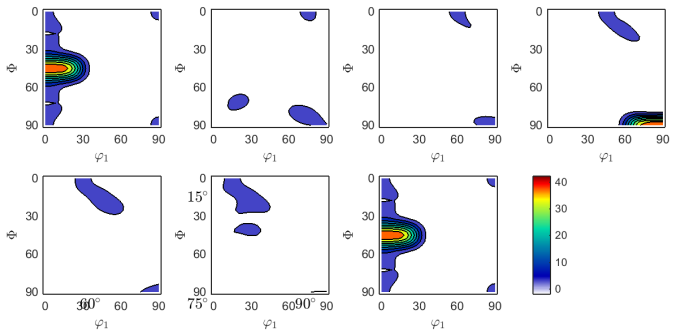

(a)

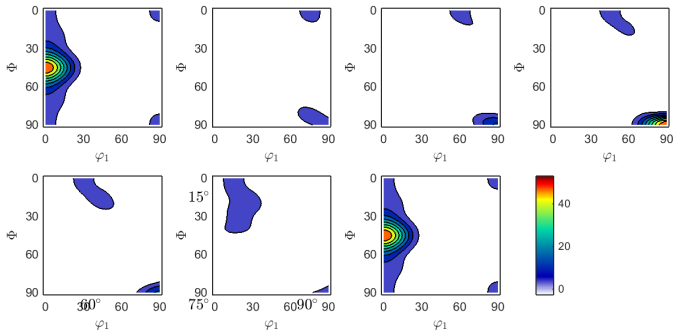

(b)

Figure 4.53: Simulated ODF for $\langle 100 \rangle$-fibre deformed using a true strain of 2. The simulation is of type IV using secant interaction scheme and a strain rate sensitivity of $m = 0.05$**(a)** and $m = 0.2$**(b)**. The deformation gradient for these simulations are plane strain as given in Table 2.5.

Figure 4.53 shows ODFs of plane strain simulation with gradients given in Table 2.5, slip system group IV, secant interaction scheme and strain rate sensitivity $m = 0.05$ for **(a)** and $m = 0.2$ for **(a)**. These simulations are the same as the ones obtained in Figure 4.52 except that the deformation mode is different. Both of these ODFs show a strong Goss components and weak Cube components.

ALAMEL Simulations

ALAMEL simulations were done using $\langle 100 \rangle$-fibre and $\langle 111 \rangle$-fibre. Slip system group I were used and relaxations were varied. These simulations are compared to VPSC simulations using slip system group I and the texture of the rolled samples.

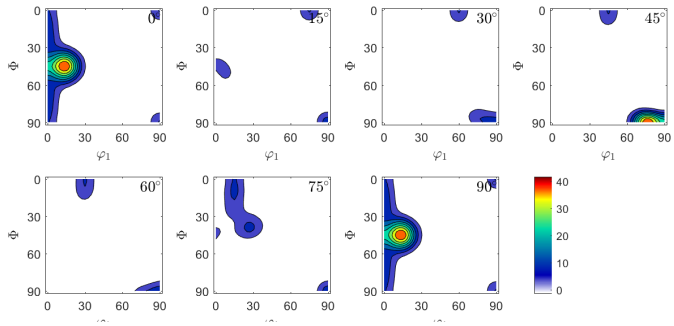

(a)

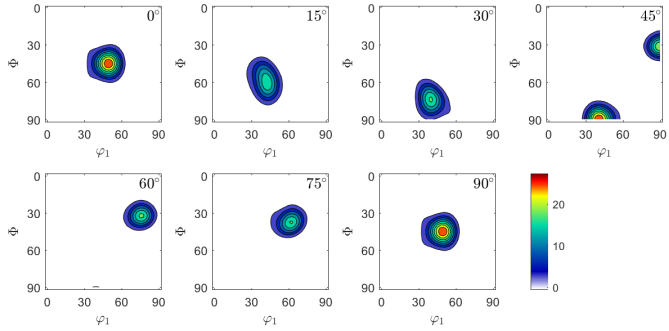

(b)

Figure 4.54: Simulated ODF for deformed **(a)**$\langle 100 \rangle$-fibre and **(b)**$\langle 111 \rangle$-fibre. The simulation uses slip system group I with the relaxation scheme is of ALAMEL Type III

Figure 4.54 shows the simulation done with ALAMEL Type III. The ODF of the deformed $\langle 100 \rangle$-fibre shows Cube and Cube-fibre and something close to Goss and α-fibre. The Cube components has an intensity of 10 times random and the peak close to Goss orientation has an intensity of 40 times random. The ODF of the deformed $\langle 111 \rangle$-fibre shows a fibre close to $\langle 111 \rangle$-fibre. The intensities are 25 times random for Brass, 15 time random for S and 15 times rand for Copper.

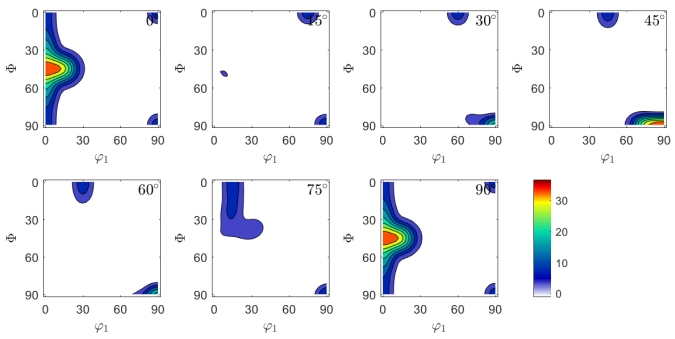

(a)

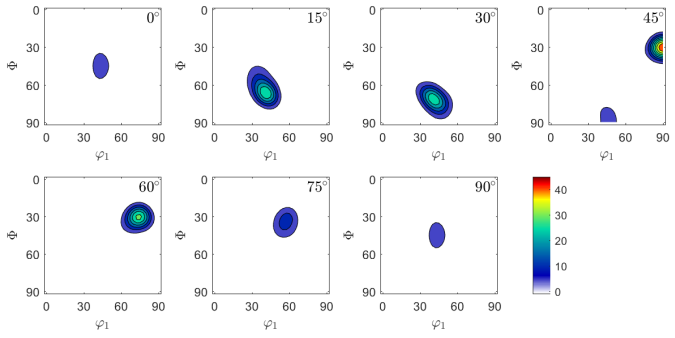

(b)

Figure 4.55: Simulated ODF for deformed **(a)**$\langle 100 \rangle$-fibre and **(b)**$\langle 111 \rangle$-fibre. The simulation uses slip system group I with the relaxation scheme is of ALAMEL

Figure 4.55 shows the ODF of the simulation done with the ALAMEL model. The deformed $\langle 100 \rangle$-fibre shows $\langle 100 \rangle$-fibre and a Goss texture component. The intensity of Cube oriented grains are 10 times random and the intensity of the Goss component are 35 times random. The deformed $\langle 111 \rangle$-fibre shows a fibre close to β-fibre. The intensities of the different components are 10 times random for Brass, 20 times random for S and 40 times random for Copper.

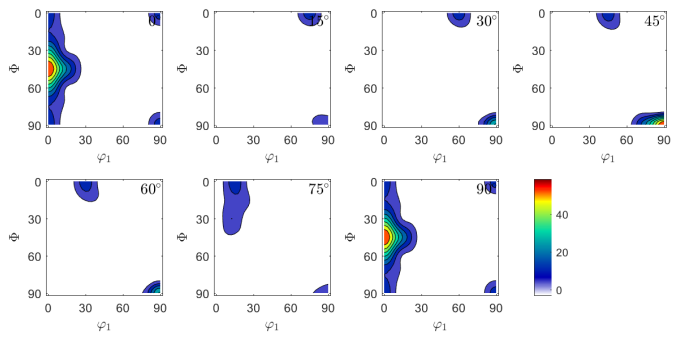

(a)

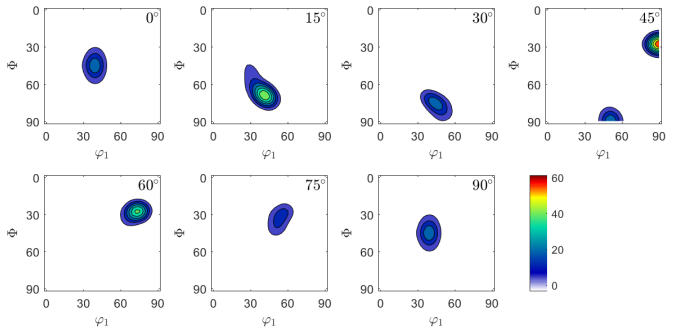

(b)

Figure 4.56: Simulated ODF for deformed **(a)**$\langle 100 \rangle$-fibre and **(b)**$\langle 111 \rangle$-fibre. The simulation uses slip system group I with FC-Taylor

Figure 4.56 shows the ODF of simulation done with using the ALAMEL software with parameters making the simulation identical to FC-Taylor. The deformed $\langle 100 \rangle$-fibre shows Cube fibre and Goss orientated grains. The intensity of the Cube orientation is 10 times random and the intensity of Goss is 50 times random. The deformed $\langle 111 \rangle$-fibre shows a β-fibre type texture. Here the intensity is 20 times random for Brass 30 times random for S and 60 times random for Copper.

Figures 6.1, 6.2, 6.3 and 6.4 show ODFs from the same simulations as the figures above except that the true strain is 1.4 instead of 1. These ODFs show the same trends as the ODFs with an elongation of 1 except that the texture is sharper.

4.2.5 Summary plane strain deformation

Simulated texture for plane strain deformation using only octahedral slip systems has been presented above. Figure 4.45 presented the different texture components for deformed $\langle 111 \rangle$-fibre. The figure failed to give a good picture for the intensities along the texture fibre in the simulated ODFs. This is because the fibre intensities are obtained using exact orientations for each component. Since few of the simulated textures were able to develop from a $\langle 111 \rangle$-fibre into a β-fibre, does Figure 4.45 give a small value for Brass and Copper

components.

Figure 4.57 presents the texture components for experimental extruded flat profile, and rolled samples and simulations using slip system group I (just close packed slip systems). The values are obtained from the different ODFs. The intensity of the different texture components are not obtained using the exact orientation of the components. Instead are values the intensities of the observed fibre component having Φ is equal to Φ of the components noted in Figure 4.57.

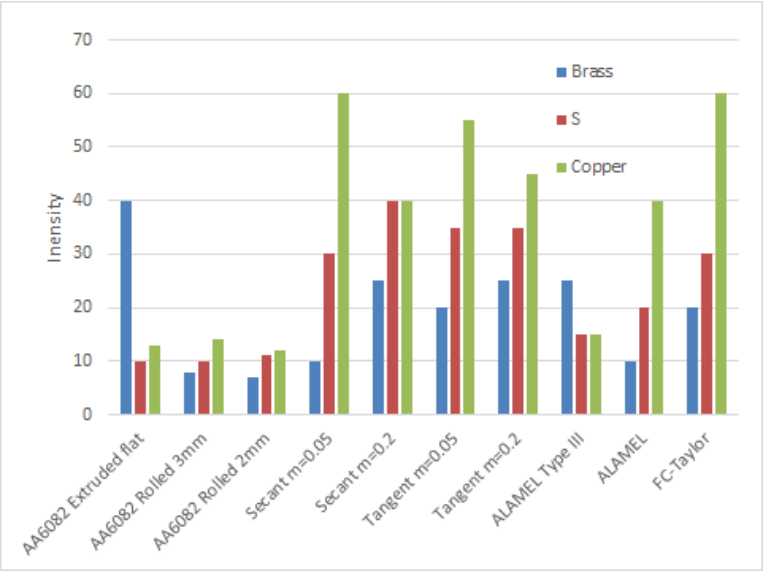

Figure 4.57: Intensities of the texture components of β-fibre in the experimental textures (extrusion of flat profile and rolling) and the simulated textures using plane strain deformation with $\langle 111 \rangle$-fibre as input fibre. The simulation used slip system group I.

Figure 4.57 compares the intensity of different texture components along the β-fibre for both experimental and simulated textures. The extruded flat profile are deformed at high temperatures and has Brass as the strongest component (in the β-fibre) followed by S and Copper as the weakest. Both rolled textures show Brass as the weakest component followed by S and Copper as the strongest. These samples were deformed at low temperatures. The simulated textures mostly show Brass as the weakest component followed by S and copper as the strongest. An exception to this is the simulations using ALAMEL Type III.

Chapter 5

Discussion

The discussion part is divided into four sections. The first section discusses the microstructure and texture in AA6082 extruded flat profile and the AA6082 extruded cylindrical rod. The results will be compared to the low temperature extrusion counterparts studied in the COSMETEX project. The microstructure and texture trough the thickness are also discussed. The other sections are uni-axial tensile strain, plane strain and recrystallization. The uni-axial tensile strain section compares the AA6082 extruded cylindrical rod to the simulations done with the simulations done using the deformation gradients of uni-axial tensile strain .

The plane strain section is divided into low temperature deformation and high temperature deformation. For low temperature deformation the experimental basis is the rolled plates. These are compared with the simulations where only the slip systems containing the close-packed slip planes are activated. The interaction schemes and strain rate sensitivity are varied for all simulations. The low temperature plane strain deformation simulations are the simulations best suited for comparing the interactions scheme and rate sensitivity. This is because they only uses one slip system group. This means that the simulation has less parameters that are varied and it is therefore easier to pinpoint the contribution of the interaction scheme and rate sensitivity. High temperature plane strain deformations use the extruded flat profile as basis even though the extruded flat profile does not only experience pure uni-axial tensile deformation and pure plane strain as seen in Chapter 4.2.1. The simulations used in this comparison are the simulation done with plane strain deformation gradients and modified plane strain deformation gradients. The main goal of these simulations is to examine how one can get the Cube component which is observed in the extruded flat profile.

The recrystallization section compares the rolled samples after annealing. The main goal of this is to examine what recrystallization texture is obtained and if annealing temperature and alloy composition influence the recrystallization texture and microstructure.

5.1 Experimental deformation microstructure after high temperature extrusion and after subsequent cold rolling

Both the extruded flat profile and extruded cylindrical rod of AA6082 show a deformed microstructure. The AA6060 round profile shows a recrystallised microstructure. The fast recrystallisation has also been observed in AA6063 round profile studied in COSMETEX project. The static recrystallisation at the end of extrusion of AA6060 and AA6063 materials is very fast and could finish within 2 seconds (Zhang et al. (2015). The spontaneous recrystallisation is attributed to high deformation and annealing temperature and no dispersoids. The AA6082 contains dispersoids which prevent recrystallisation.

The cylindrical round profile extruded at 500°C shows a defomrmed texture containing close to 0.5 $\langle 100 \rangle$-fibre and 0.43 $\langle 111 \rangle$-fibre. A texture containing these fibres has been reported for low temperature (300°C) extrusion of AA6063 round profiles (Zhang et al. (2015) where the fraction of $\langle 111 \rangle$-fibre was about four times higher than the fraction of $\langle 100 \rangle$-fibre. This indicate that an increase in temperature can lead to a increase in the fraction of $\langle 100 \rangle$-fibre obtained in uni-axial deformation.

The centre of the AA6082 extruded flat profile extruded at 500°C had a texture consisting of Cube components and β-fibre. The Cube has an intensity of 25 times random. Brass component is the strongest texture component in the β-fibre followed by Copper and S. Flat profile extruded at low temperature (350°C) has also been studied in COSMETEX project (unpublished results). The deformation texture of low temperature extrusion showed little Cube (intensity of 2 times random). The β-fibre in this texturre was strongest at Copper, second strongest at S and weakest at Brass. This indicate that Cube texture component is a product of high temperature extrusion

The influence of extrusion temperature on the deformation texture could be attributed to many factors for example instantaneous strain-rate sensitivity, grain interactions, deformation mechanisms etc. The increasing strain-rate sensitivity at higher temperature could delay the evolution of deformation texture (s Mánik and Holmedal (2014). When deformed at high temperature, the grain interactions among grains might be different than at low temperature. At higher temperatures can non octahedral activate which can influence the deformation texture (Pérocheau and Driver (2000). VPSC simulations will be discussed to find if some of these factors could be used to explain the difference between the high temperature deformation and low temperature deformation.

The AA6060 extruded round profile shows a $\langle 100 \rangle$-fibre texture. This will evolve into a Goss component and slightly towards a Brass component (as in an α-fibre). The strength of the Goss increases with increased rolling strains. The AA6082 extrudedd round profile contains both $\langle 100 \rangle$-fibre and $\langle 111 \rangle$-fibre. The $\langle 100 \rangle$-fibre will evolve into Goss texture as it does for AA6060. The observed β-fibre are therefore a product of the deformed $\langle 111 \rangle$-fibre.

The microstructures and texture in the AA6082 extruded flat profile (Having a thickness of 10 mm) shows some through thickness variations. The area closest to the surface shows a recrystallised microstructure. The material here are recrystallised because of the large strains the material closest to the surface experiences during the extruding process. The deformed area, close to the large recrystallised grains, shows an unsymmetrical texture. This unsymmetrical texture lies in the area 400 μm to 1000 μm into the sample. The

unsymmetrical texture is a product of the shear strains the material closer to the surface experienced. The area going from 1 mm into the surface to the centre has little (5 mm from surface) variations in microstructure. The symmetrical texture observed in this area indicate that this area does not experience much shear strain. Overall does the shear strain only influence the texture from the surface and 1 mm into the 10 mm thick extruded flat profile.

5.2 Uni-axial tensile strain

The experimental deformation texture from the extruded rod has close to 0.5 $\langle 100 \rangle$-fibre and 0.43 $\langle 111 \rangle$-fibre. The simulations using only the $\{111\}\langle 110 \rangle$ slip system, which are applied for cold working, give lower fraction of $\langle 100 \rangle$-fibre and higher fraction $\langle 111 \rangle$-fibre. When using the tangent interaction scheme and a strain rate sensitivity of 0.2 we can observe a increase in the fraction of $\langle 100 \rangle$-fibre and a decrease in the fraction of $\langle 100 \rangle$-fibres. There are also a slight increase when using the same interaction scheme and a strain rate sensitivity of 0.05. This means that the tangent interaction scheme might promote $\langle 100 \rangle$-fibres especially at higher strain rate sensitivities.

The slip system group which promotes the $\langle 100 \rangle$-fibre during uni-axial strain the most is slip system group III where the $\{112\}\langle 110 \rangle$ slip system is included. Here the fraction of $\langle 100 \rangle$-fibres is close to 0.5. The secant interaction scheme is the interaction scheme that promotes $\langle 100 \rangle$-fibres the most when using slip system group III. This is not the case when using other slip system groups. The tangent interaction scheme does not promote the $\langle 100 \rangle$-fibres for this slip system group as it did with slip system group I. Here the tangent interaction scheme seams to decrease the fraction of $\langle 100 \rangle$-fibres compared to using the secant interaction scheme.

Among the simulations carried out using ALAMEL slip system group III is the simulation that promotes $\langle 100 \rangle$-fibre the most. The simulations of type ALAMEL and ALAMEL Type III has lower amount of $\langle 100 \rangle$-fibre than the simulation which is identical to FC-Taylor. This may indicate that relaxations of shear plane do not improve the amount of $\langle 100 \rangle$-fibre and further solidify that the activation of the $\{112\}\langle 110 \rangle$ slip system is responsible for the high friction of $\langle 100 \rangle$-fibre.

Slip system group IV and II gives a fraction of $\langle 100 \rangle$-fibres which is lower than the fraction obtained by not including an extra slip system.

5.3 Plane strain deformation

5.3.1 Low temperature deformation

The rolled AA6082 plate rolled down to 3 mm can be compared to the simulations done with a true strain of 1. The texture of the rolled plate, before rolling, consisted of around 0.5 $\langle 111 \rangle$-fibre and 0.5 $\langle 100 \rangle$-fibre. It is assumed that the texture after rolling will be 0.5 rolled $\langle 111 \rangle$-fibre and 0.5 rolled $\langle 100 \rangle$-fibre. This means that the deformed texture will have peaks equal to half of what it would have if it was pure deformed $\langle 111 \rangle$-fibre and $\langle 100 \rangle$-fibre. The comparison can easily be done since the deformed textures of these

to fibres have no common orientation peaks in the ODF. The difference between the input fibres for simulation and the fibres obtained experimentally is that the input fibres are sharper than those obtained experimentally. This leads to a uncertainty regarding the values in the ODF, but there is no problem in comparing the relative densities and orientations in an ODF to other ODFs.

For the rolled AA6060 plate the starting texture 0.6 $\langle 100 \rangle$-fibre with the rest being random texture. This means that we can compare the simulation of deformed $\langle 100 \rangle$-fibre with the texture obtained from the rolled AA6060 plates. Here we also have to assume that the simulated textures are stronger than the experimental textures.

The simulated rolled $\langle 111 \rangle$-fibres all has ODFs showing a fibre texture where the fibre is close in position to the original $\langle 111 \rangle$-fibre. A difference between the simulations using different simulation schemes is that the simulations using the tangent interaction scheme is closer to the $\langle 111 \rangle$-fibre whereas the simulations using secant interaction scheme is closer to the β-fibre. The experimental rolled AA6082 plate has the fibre closer to the β-fibre, meaning that the secant interaction scheme is better than the tangent interaction scheme in this regard. The simulations done, using the ALAMEL simulation software, that correspond best with the experimental results, with regards to the orientations of this fibre, are the FC-Taylor simulations. This gives good agreement with the fact that the simulations done in VPSC with the secant interaction scheme are closer to FC-Taylor than the simulations done with the tangent interaction scheme.

Almost all simulations give the distribution of the different component of the fibre where intensity of Copper is higher than the intensity of S which again is higher than the intensity of Brass (Figure 4.57). The experimental texture of the rolled extruded round AA6082 material also show the same relationship between the components of the β-fibre where Copper has the highest intensity followed by S and Brass. The simulated texture has higher intensities than the experimental is common. The simulation using Secant and strain rate sensitivity of 0.2 differs from the rest of the simulations having a weaker Copper component, however are the other components of this simulation as expected. The simulation using ALAMEL Type III has a texture which do not correspond with the cold deformed experiments at all. This means that all simulations except VPSC using secant interaction scheme and strain rate sensitivity of 0.2 and ALAMEL Type 3 give good prediction of the intensity distribution along the β-fibre in the ODFs.

Overall do the VPSC simulation using secant interaction scheme and low strain rate sensitivity and the simulation identical to FC-Taylor predict the deformation of the $\langle 111 \rangle$-fibre the best. VPSC simulations using secant interaction scheme approaches FC-Taylor when strain rate sensitivity goes towards zero. This means that it makes sense that these two simulations has similar results.

5.3.2 High temperature deformation

The plane strain simulations of the deformed $\langle 100 \rangle$-fibre shows Goss and Cube components both by use of non-octahedral slip systems and octahedral slip systems. The difference between the simulations with different slip systems and different strain rate sensitivity lies mainly in how the intensities of these two texture components varies. According to Arzaghi et al. (2009) inclusion of non-octahedral slip systems gives slower evolution of the deformation texture, but no change in the end texture. Both the simulations and the

experiments show that this means lower intensity of Goss components and more even intensities along the $\langle 100 \rangle$-fibre. This also means a higher intensity of Cube components. The problem with these results is that they do not remove Goss components, which is non-existent in the texture obtained experimentally from the extruded flat profile.

Figure 4.3 is the only experimental ODF from a deformation containing plane strain done at elevated temperatures. The velocity gradients for this deformation is assumed to be close the deformation given in Figure 4.40 and Table 4.1. The texture evolution during extrusion is expected to be similar to that of the extruded rods during the first part of the deformation. This means that the texture will be 0.5 $\langle 100 \rangle$-fibre and 0.5 $\langle 111 \rangle$-fibre at one point during the deformation before it is exposed to deformation mode which is more like plane strain.

The experimental end textures for extrusion of flat profiles show strong Cube components and no Goss components. This is not observed in any of the simulations done with the deformation velocity gradients in Table 2.5 (plane strain) where deformation of the $\langle 100 \rangle$-fibre gives more Goss components and less Cube components. By modifying the deformation velocity gradients into the gradients shown in Table 3.2 (modified plane strain), there are possible to get texture containing strong cube and no Goss. This is done by including the $\{110\}\langle 110 \rangle$ slip system and using the secant interaction scheme. Both simulations using these velocity gradients, slip system group IV and the secant interactions scheme gives Cube as the strongest texture component with no (or little) Goss components. The Goss component has rotated to a β-fibre where the Brass component is strongest. The Brass component has an intensity which is a somewhat lower than the Cube component.

The resulting ODFs from the high temperature deformation simulations, where the $\langle 111 \rangle$-fibre is deformed, show a β-fibre just as it did for octahedral slip systems. Here is also the Cu component the strongest component, the S component the second strongest and Brass being the weakest. This is contrary findings to the β-fibre obtained experimentally at high temperature were Brass is the strongest component followed by Copper and S. Some of the Brass component observed in the texture of the flat profile originates from the $\langle 100 \rangle$-fibre. Since this β-fibre has Brass components as the strongest component, the aggregate between the simulations of the deformed $\langle 100 \rangle$-fibre and $\langle 111 \rangle$-fibre will have a β-fibre which are closer to the one observed in the experimental flat profile.

The results indicate that we can not attribute the strong Cube components observed for flat extruded profiles to activation of non-close packed slip systems when using plane strain deformation. The strong Cube components might be attributed to the activation of the $\{110\}\langle 110 \rangle$ slip system when using the modified plane strain deformation as given in Table 3.2. An experiment using hot deformation plane strain can gain knowledge about the possibility of obtaining the texture with strong Cube components during plane strain. If that is the case the non-close packed slip system is not the reason for the strong Cube components after plane strain compression.

5.4 Recrystallization

Both AA6060 and AA6082 were recrystallised after rolling and annealing at both 450°C and 550°C for 100 s. The ODFs samples show a weak texture for all samples except the AA6060 sample rolled to 2 mm and annealed at 550°C. The strong texture in this sample

is probably because of the large grains present in the sample.

Grain sizes with standard deviations are illustrated in Figure 5.1. The AA6060 alloys have larger grains than AA6082 for all annealing temperatures and all deformations. AA6082 shows slightly larger grains when the annealing temperature are higher. This is more pronounced in the AA6060 alloy. The AA6060 sample annealed for 10 more minutes show a larger grains than the sample only annealed for 10 s. From the IPF-micrograph can it be observed that the grains near the centre are a bit larger than the grains towards the sides. The difference in grain size, between the sample annealed for 10 s and the sample annealed for 10 s + 10 minutes, might indicate further grain growth after recrystallization.

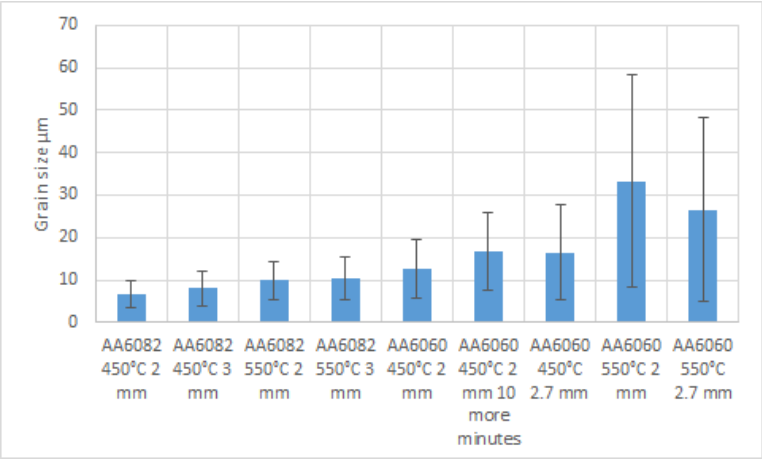

Figure 5.1: Grain sizes after annealing with standard deviation.

The fine grains of the annealed AA6082 samples mean that we can be quite confident in the texture obtained from these samples. These textures show a lot of random orientated grains, but there are also some texture components in the samples that is common for all samples. One of these texture components is 20°ND-rotated Cube. These texture components along with the weak texture correspond well with the recrystallization texture commonly obtained from PSN (Engler et al. (1997). PSN might be due to existence of large constituent particles. The difference between the samples annealed at 450°C and the samples annealed at 550°C is that the samples annealed at 450°C has a stronger β-fibre along with higher intensity of the other fibre observed at $\phi_2 = 0°$.

Chapter 6

Conclusions

In this thesis the deformation texture and microstructure of extruded and rolled AA6060 and AA6082 were analysed by EBSD and XRD. Crystal plasticity simulations using VPSC where done where the deformation gradients were uni-axial tensile deformation and plane strain deformation. Active slip systems, interaction scheme and rate sensitivity were varied in these simulations.

- The centre of extruded flat profile of AA6082, having a thicknes of 10 mm, has a texture dominated by Cube and β-fibre. There are little variations in texture and microstructure in the area from the centre (5 mm from surface) to 10 mm from surface.

- The area near the surface (400 μm to 1000 μm) has an unsymmetrical deformed texture. The are closest (0-400 μm) has a recrystallised microstructure with large grains. The subgrain size in this area are 9.9 ± 4.4 μm. Th

- The centre of extruded cylindrical rod of AA6082 has 0.43 $\langle 111 \rangle$-fibre an 0.5 $\langle 100 \rangle$-fibre.

- Cold rolling of extruded cylindrical AA6082 rod, containing $\langle 100 \rangle$-fibre and $\langle 100 \rangle$-fibre texture, gives β-fibre and Goss texture.

- Annealing of rolled AA6082 and AA6060 gives a weak recrystallised texture which is equal to texture usually obtained from PSN.

- VPSC simulation with the inclusion of the $\{112\}\langle 110 \rangle$ slip system is the simulations that predict the texture of extruded cylindrical rods the best. This is because the $\{112\}\langle 110 \rangle$ promotes $\langle 100 \rangle$-fibre.

- Tangent interaction scheme and high rate sensitivity promotes $\langle 100 \rangle$-fibre with uni-axial tensile deformation.

- Comparing cold rolled texture with VPSC simulations of deformation of $\langle 111 \rangle$-fibre indicates that the secant interaction scheme having low strain rate sensitivity gives better simulation results for plane strain than the tangent interaction scheme.
- Inclusion of more slip system does not promote Cube components at the expense of Goss components when plane strain deformation are used. This indicates that activation of non-octahedral slip systems are not the reason for Cube components in extruded flat profiles.
- Modifying the plane strain deformation as shown in Table 3.2 gives Cube components at the expense of Goss when the $\{110\}\ \langle 110 \rangle$ is included in the simulations.

6.1 Recommendations of further work

Recommended future work includes plane strain deformation at elevated temperatures of an AA6082 sample containing $\langle 100 \rangle$-fibre and $\langle 111 \rangle$-fibre to examine if one can obtain a texture with Cube components and no Goss components. This can be carried out by first extruding the sample into a rod and then performing the hot rolling.

A similar experiment using machinery which creates a deformation gradient as shown in Table 3.2 could also be done.

Simulations can be carried out using deformation modes which a extruded flat profile experiences(Table 4.1), having the active slip system being combinations of the $\{111\}\ \langle 110 \rangle$, $\{112\}\ \langle 110 \rangle$ and $\{110\}\ \langle 110 \rangle$ slip systems. This can be done for comparison to the simulations done in this work using a to step approach and in comparison to the experimental textures.

Bibliography

aalco.co.uk, may 2016a. Aluminium alloy - commercial alloy - 6060 - t5 extrusions.
URL http://www.aalco.co.uk/datasheets/Aluminium-Alloy-6060-T5--Extrusions_144.ashx

aalco.co.uk, may 2016b. Aluminium alloy - commercial alloy - 6082 - t6 t651 plate.
URL http://www.aalco.co.uk/datasheets/Aluminium-Alloy-6082-T6T651-Plate_148.ashx

AluMatter, june 2016.
URL http://aluminium.matter.org.uk/content/html/eng/default.asp?catid=99&pageid=1028022659

Andersen, S. J., Zandbergen, H. W., Jansen, J., Træholt, C., Tundal, U., Reiso, O., 1998. The crystal structure of the phase in almgsi alloys. Acta Materialia 46 (9), 3283–3298.

Arzaghi, M., Beausir, B., Tth, L., 2009. Contribution of non-octahedral slip to texture evolution of fcc polycrystals in simple shear. Acta Materialia 57 (8), 2440 – 2453.
URL http://www.sciencedirect.com/science/article/pii/S1359645409000664

Azari, H. N., Wilkinson, D. S., Girard, S. X., Lloyd, D. J., 2004. Effect of thermomechanical treatment on the evolution of rolling and recrystallization textures in twin-belt cast aa5754 aluminum alloy. Metallurgical and Materials Transactions A 35 (6), 1839–1851.

Beevers, C., Honeycombe, R., 1961. Cubic slip in aluminium alloy crystals. Acta Metallurgica 9 (5), 513 – 515.

Burke, J., Turnbull, D., 1952. Recrystallization and grain growth. Progress in metal physics 3, 220–292.

Caillard, D., Martin, J.-L., 2009. Glide of dislocations in non-octahedral planes of fcc metals: a review. International Journal of Materials Research 100 (10), 1403–1410.

Couret, A., Caillard, D., 1988. Microscopic observations of glide in non close-packed planes in aluminium, and comparison with magnesium. Acta Metallurgica 36 (9), 2515 – 2524.

Davis, J. R., Davis, J. R., 1993. Aluminum and aluminum alloys. ASM international.

Dieter, G. E., 2015. Mechanical metallurgy. McGraw-Hill Book Company.

Doherty, R. D., Hughes, D. A., Humphreys, F. J., Jonas, J. J., Jensen, D. J., Kassner, M. E., King, W. E., McNelley, T. R., McQueen, H. J., Rollett, A. D., 1997. Current issues in recrystallization: a review. Materials Science and Engineering: A 238 (2), 219–274.

Duckham, A., Engler, O., Knutsen, R. D., 2002. Moderation of the recrystallization texture by nucleation at copper-type shear bands in al-1mg. Acta Materialia 50 (11), 2881–2893.

Edwards, G., Stiller, K., Dunlop, G., Couper, M., 1998. The precipitation sequence in al–mg–si alloys. Acta Materialia 46 (11), 3893–3904.

Engler, O., 2003. Through-process modelling of the impact of intermediate annealing on texture evolution in aluminium alloy aa 5182. Modelling and Simulation in Materials Science and Engineering 11 (6), 863.

Engler, O., Kong, X., Yang, P., 1997. Influence of particle stimulated nucleation on the recrystallization textures in cold deformed al-alloys part iexperimental observations. Scripta Materialia 37 (11), 1665 – 1674.

Furu, T., Vatne, H. E., 1998. Texture evolution during extrusion of flat aa6060 and aa6082 aluminium profiles. In: Materials science forum. Vol. 273. Trans Tech Publ, pp. 403–410.

Fylkesnes, H., dec 2015. Microstructure and texture in extruded profiles.

Gottstein, G., 2004. Physical foundations of materials science. Springer Science & Business Media.

Goyal, A., 2011. Strong, non-magnetic, cube textured alloy substrates.
URL `http://www.google.com/patents/US7879161`

Hasting, H. S., Frøseth, A. G., Andersen, S. J., Vissers, R., Walmsley, J. C., Marioara, C. D., Danoix, F., Lefebvre, W., Holmestad, R., 2009. Composition of β precipitates in al–mg–si alloys by atom probe tomography and first principles calculations. Journal of Applied Physics 106 (12), 123527.

Hazif, R. L., Poirer, J.-P., 1975. Cross-slip on 110 planes in aluminum single crystals compressed along 100 axis. Acta Metallurgica 23 (7), 865 – 871.

Hirsch, J., Lücke, K., 1988. Overview no. 76. Acta Metallurgica 36 (11), 2883–2904.

Hjelen, J., rsund, R., Nes, E., 1991. On the origin of recrystallization textures in aluminium. Acta Metallurgica et Materialia 39 (7), 1377 – 1404.

Hong, S.-H., Lee, D. N., 2003. The evolution of the cube recrystallization texture in cold rolled copper sheets. Materials Science and Engineering: A 351 (12), 133 – 147.

Houtte, P. V., Li, S., Seefeldt, M., Delannay, L., 2005. Deformation texture prediction: from the taylor model to the advanced lamel model. International Journal of Plasticity 21 (3), 589 – 624.

Hu, R., Ogura, T., Tezuka, H., Sato, T., Liu, Q., 2010. Dispersoid formation and recrystallization behavior in an al-mg-si-mn alloy. Journal of Materials Science & Technology 26 (3), 237–243.

Humphreys, F. J., Hatherly, M., 2004. Chapter 12 - Recrystallization Textures. Elsevier, Oxford, pp. 379–413.

Lebensohn, R., Tomé, C., 1993. A self-consistent anisotropic approach for the simulation of plastic deformation and texture development of polycrystals: application to zirconium alloys. Acta metallurgica et materialia 41 (9), 2611–2624.

Lücke, K., Rixen, R., Senna, M., 1976. Formation of recrystallization textures in rolled aluminum single crystals. Acta Metallurgica 24 (2), 103–110.

Mánik, T. s., Holmedal, B., 2013. Additional relaxations in the alamel texture model. Materials Science and Engineering: A 580, 349–354.

Marioara, C., Andersen, S., Zandbergen, H., Holmestad, R., 2005. The influence of alloy composition on precipitates of the al-mg-si system. Metallurgical and Materials Transactions A 36 (3), 691–702.

Marioara, C., Nordmark, H., Andersen, S., Holmestad, R., 2006. Post-β phases and their influence on microstructure and hardness in 6xxx al-mg-si alloys. Journal of materials science 41 (2), 471–478.

Matsuda, K., Sakaguchi, Y., Miyata, Y., Uetani, Y., Sato, T., Kamio, A., Ikeno, S., 2000. Precipitation sequence of various kinds of metastable phases in al-1.0 mass% mg2si-0.4 mass% si alloy. Journal of materials science 35 (1), 179–189.

Miao, W. F., Laughlin, D. E., 1999. Precipitation hardening in aluminum alloy 6022. Scripta Materialia 40 (7), 873–878.

Oosterkamp, L. D., Ivankovic, A., Venizelos, G., 2000. High strain rate properties of selected aluminium alloys. Materials Science and Engineering: A 278 (12), 225 – 235.

Paulsen, C. O., jun 2015. Recrystallisation behaviour in extruded profiles of non-dispersoid containing al-mg-si alloys. Master's thesis, NTNU.

Pérocheau, F., Driver, J., 2000. Texture gradient simulations for extrusion and reversible rolling of fcc metals. International Journal of Plasticity 16 (1), 73–89.

Reiso, O., 2004. Extrusion of almgsi alloys. In: Materials Forum. Vol. 28. Citeseer, pp. 32–46.

Reiso, O., 2015. Tmt4266, metal fabrication and forming- microstructure and crystal plasticity- extrusion & metallurgy, 2015.

s Mánik, T., Holmedal, B., 2014. Review of the taylor ambiguity and the relationship between rate-independent and rate-dependent full-constraints taylor models. International Journal of Plasticity 55, 152 – 181.

Tomé, C. N., 1999. Self-consistent polycrystal models: a directional compliance criterion to describe grain interactions. Modelling and Simulation in Materials Science and Engineering 7 (5), 723.

Verlinden, B., Cahn, R. W., 2007. Thermo-mechanical processing of metallic materials. Pergamon, London.

Verlinden, B., Driver, J., Samajdar, I., Doherty, R. D., 2007. Thermo-mechanical processing of metallic materials. Vol. 11. Elsevier.

Verlinden, B., Suhadi, A., Delaey, L., 1993. A generalized constitutive equation for an aa6060 aluminium alloy. Scripta Metallurgica et Materialia 28 (11), 1441 – 1446.

Zhang, K., Pettersen, T., Paulsen, C., Marthinsen, K., Holmedal, B., Segatori, A., 2015. Recrystallization behaviour of aa6063 extrusions. In: IOP Conference Series: Materials Science and Engineering. Vol. 89. IOP Publishing, p. 012057.

Appendix

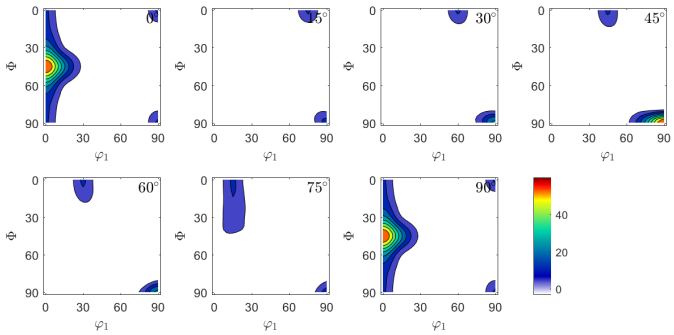

(a)

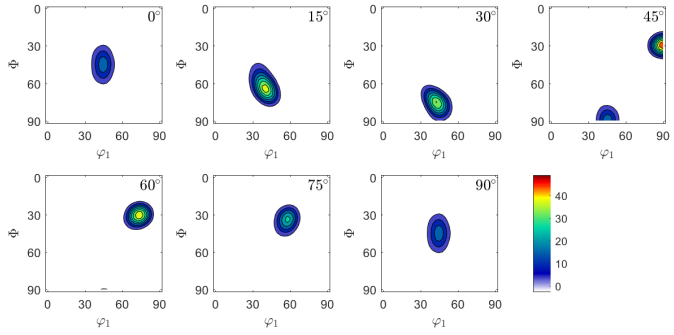

(b)

Figure 6.1: Simulated ODF for deformed $\langle 100 \rangle$-fiber and $\langle 111 \rangle$-fiber with a total elongation of 1.4. The simulation is of type I with VPSC. The interaction scheme was secant and rate sensitivity was 0.2

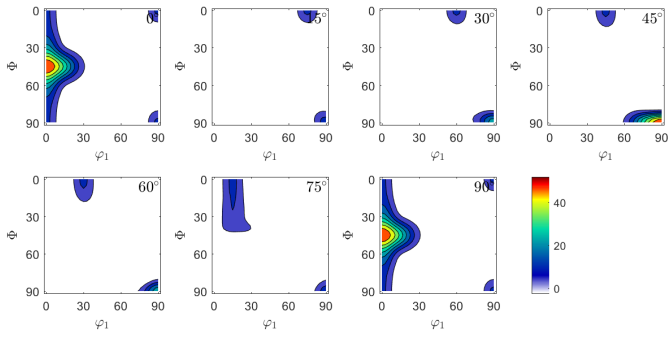

(a)

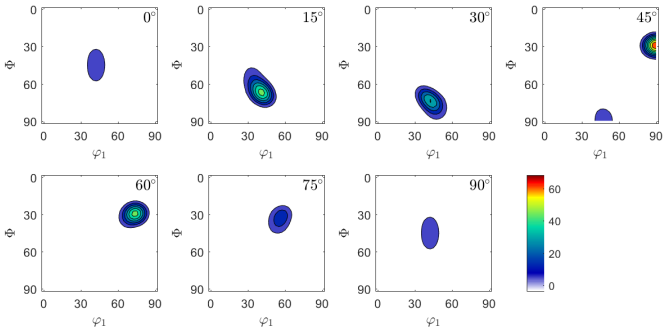

(b)

Figure 6.2: Simulated ODF for deformed ⟨100⟩-fiber and ⟨111⟩-fiber with a total elongation of 1.4. The simulation is of type I with VPSC. The interaction scheme was secant and rate sensitivity was 0.05

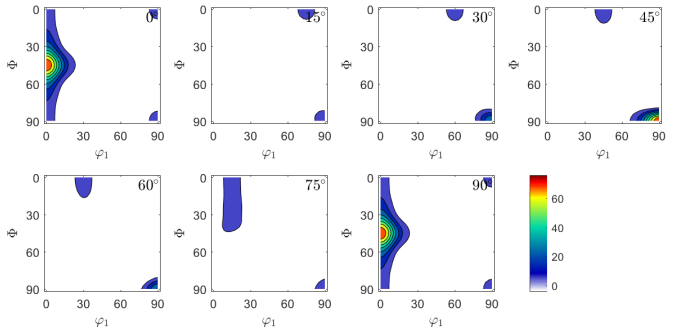

(a)

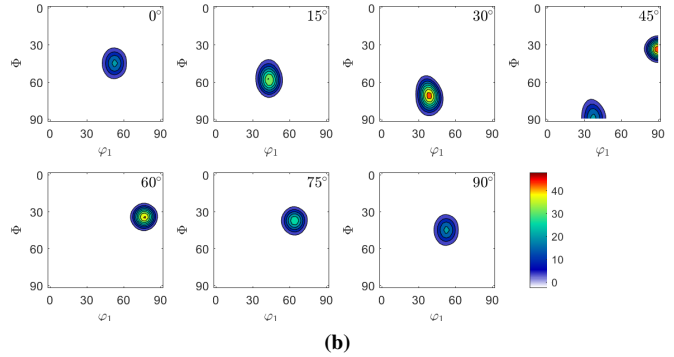

(b)

Figure 6.3: Simulated ODF for deformed ⟨100⟩-fiber and ⟨111⟩-fiber with a total elongation of 1.4. The simulation is of type I with VPSC. The interaction scheme was tangent and rate sensitivity was 0.2

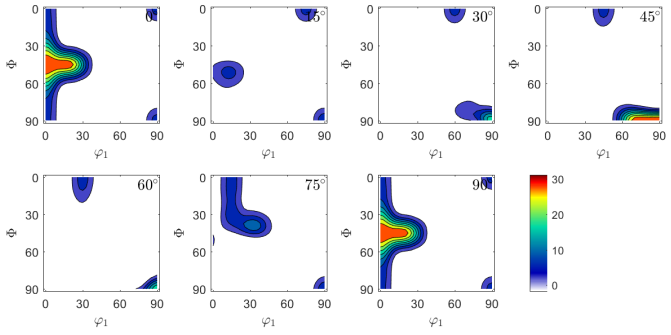

(a)

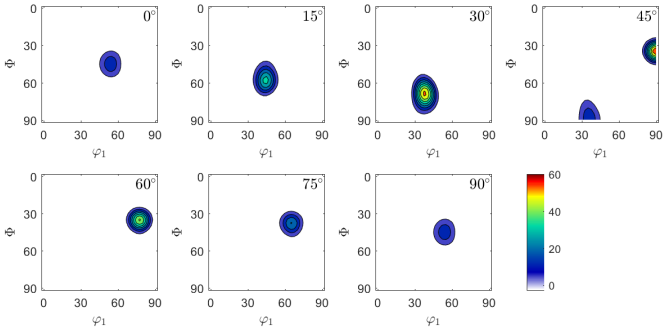

(b)

Figure 6.4: Simulated ODF for deformed ⟨100⟩-fiber and ⟨111⟩-fiber with a total elongation of 1.4. The simulation is of type I with VPSC. The interaction scheme was tangent and rate sensitivity was 0.05